

# Supporting Information

## **Light Activation and Photophysics of a Structurally Constrained Nickel(II)-Bipyridine Aryl Halide Complex**

Daniel Bím,<sup>a,b</sup> Kaitlin M. Luedecke,<sup>a</sup> David A. Cagan,<sup>a</sup> Ryan G. Hadt<sup>a,\*</sup>

<sup>a</sup>Division of Chemistry and Chemical Engineering, Arthur Amos Noyes Laboratory of Chemical Physics, California Institute of Technology, Pasadena, California 91125, United States

<sup>b</sup>Institute of Organic Chemistry and Biochemistry, The Czech Academy of Sciences, Flemingovo nám. 2, Prague 6 166 10, Czech Republic

\*Corresponding Author: [rghadt@caltech.edu](mailto:rghadt@caltech.edu)

## Table of Contents

<b>S1.</b>	<b>Experimental Section .....</b>	<b>S3</b>
S1.1.	General Considerations.....	S3
S1.2.	Synthetic Details.....	S4
S1.3.	Steady-State UV-vis Spectroscopy.....	S9
S1.4.	Photolysis Experiments .....	S10
S1.5.	Kinetic Modeling.....	S23
S1.6.	Transient Absorption Spectroscopy.....	S24
<b>S2.</b>	<b>Computational Section.....</b>	<b>S29</b>
S2.1.	General Computational Considerations.....	S29
S2.2.	Electronic Structure Calculations .....	S30
<b>S3.</b>	<b>References .....</b>	<b>S38</b>
<b>S4.</b>	<b>NMR Spectra .....</b>	<b>S40</b>
<b>S5.</b>	<b>XYZ Structures .....</b>	<b>S45</b>

## S1. Experimental Section

### S1.1. General Considerations

All purchased chemicals were used as received unless otherwise noted. Bis-(1,5-cyclooctadiene)nickel(0) was purchased from Strem Chemicals. 2,2'-Bipyridine (bpy), bis(triphenylphosphino)(2-methylphenyl)chloronickel(II), paraformaldehyde, glacial acetic acid, ammonium acetate, acetophenone, 2'-chloroacetophenone, and mesityl bromide were obtained from MiliporeSigma. Kröhnke reagent (1-(2-oxo-2-(pyridin-2-yl)ethyl)pyridinium iodide used for synthesis of substituted bipyridine ligands was purchased from Fisher Scientific. Air sensitive solids were dried under vacuum and brought into a nitrogen-atmosphere glovebox; liquids were degassed via freeze-pump-thaw technique and brought into the glovebox, and stored over 3 Å molecular sieves. All solvents were air-free and collected from the solvent purification system (SPS), then stored in the glovebox over 3 Å molecular sieves. Tetrahydrofuran (THF) was inhibitor-free. Complex **1** was prepared following a literature procedure in ref 1, and 6-phenyl-2,2'-bipyridine, 6-(2-chlorophenyl)-2,2'-bipyridine, and complex **2** in ref 2 (details below).

UV-vis absorption spectra of the complexes were collected on a Varian Cary 500 spectrophotometer using Starna Cells air free 6-Q 10 mm path length cuvettes. Heating/decomposition kinetics were acquired on a UV-vis HP Agilent 8453 spectrophotometer coupled to an HP 89090A Peltier temperature controller with a cell holder. Deuterated solvents were purchased from Cambridge Isotope Laboratories. Deuterated methylene chloride was stored over activated 3 Å molecular sieves in a nitrogen-filled glovebox. Proton nuclear magnetic resonance ( $^1\text{H}$ -NMR) spectra were recorded on a 400 MHz Varian Spectrometer. Carbon nuclear magnetic resonance ( $^{13}\text{C}$ -NMR) spectra were recorded on a Bruker AV-III HD 400 MHz spectrometer.  $^{13}\text{C}$ -NMR spectra were  $^1\text{H}$  decoupled. Chemical shifts are reported in parts per million ( $\delta$  in ppm) and are referenced to the residual solvent signal (i.e.,  $\delta = 5.32$  ppm for  $\text{CD}_2\text{Cl}_2$ , 7.26 ppm for  $\text{CDCl}_3$ , and 4.79 for  $\text{D}_2\text{O}$ ). For the Evans method, a capillary tube was filled with a 20 mM stock solution of an internal standard (2-MeTHF) in  $\text{CD}_2\text{Cl}_2$  and inserted into NMR tube with a variable concentration of complex **2** (2.5 mM, 5.0 mM, 7.5 mM, 10.0 mM) and 2-MeTHF standard in  $\text{CD}_2\text{Cl}_2$ . The effective magnetic moment reported is the average of those obtained at different concentrations.

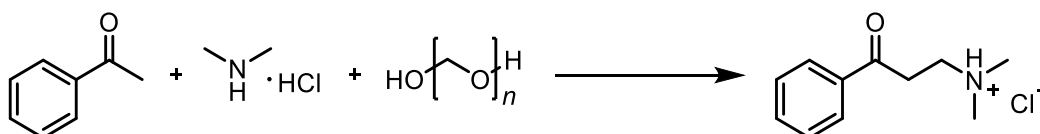
Electron paramagnetic resonance (EPR) spectroscopy was performed using a Bruker EMX X-band CW-EPR Spectrometer equipped with a ER4119HS high sensitivity resonator or ER4116DM dual mode resonator for room temperature and cryogenic experiments, respectively. Samples were prepared in Norell 4 mm air-free EPR tubes. Spectra were simulated in EasySpin simulation toolbox with MATLAB.

Photochemical stocks were prepared in a nitrogen-filled glovebox and distributed into separate spectroscopic cuvettes (Starna Cells, 10 mm path length) with air-tight seals. Each cuvette cell had volume of 2.5 mL and were placed ~5 cm away from a Kessil PR160L LED ( $\lambda_{\text{max}} = 390$  nm) to maintain the LED power of  $170 \text{ mW cm}^{-1}$  as determined with Thorlabs S425C thermal detector power meter. A cooling fan was used to maintain room temperature irradiation during the experiments.

Ultrafast transient absorption (TA) data were collected using a 1 kHz repetition rate Ti:Sapphire amplifier (Astrella, Coherent) with an output of 800 nm. The 800 nm output is passed through a beam splitter (50:50), where one line was passed through another beam splitter (90:10) and frequency doubled through a  $\beta$ -barium borate (BBO) nonlinear optical crystal (EKSMA Optics, 10 mm x10 mm x 0.2 mm,  $\theta = 29.2^\circ$ ,  $\phi = 90^\circ$ , P/P@400-800 nm) to achieve 400 nm light. A fraction of the remaining 800 nm and the 400 nm pump lines were directed into a pump-probe spectrometer (Helios, Ultrafast Systems). The 800 nm beam was focused onto either a mechanically translated CaF<sub>2</sub> crystal to generate a white light continuum in the UV-visible region (~350nm – 650 nm) or onto a Sapphire crystal to generate a white light continuum in the visible region (~450 nm – 800 nm). A 450 nm longpass filter was placed after the sample and before the detector in order to minimize spectral contributions from pump scatter. Data were collected with exponential data collection from -1 ps or -0.5 ps to sufficiently long times to deduce the longest-lived excited-state lifetimes, up to 7 ns. At least 3 scans were averaged with at least 2 second averaging to give each reported spectrum.

TA samples were prepared in a nitrogen-filled glovebox using 2 mm Schlenk quartz cuvettes. Concentrations were adjusted to give maximum UV-vis absorbance values of ~0.7 across the spectrum. UV-vis spectra were collected before and after each sample measurement to ensure no photodegradation. Global fitting of transient absorption kinetic data was achieved with the R package *TIMP*<sup>3</sup> and Glotaran.<sup>4</sup> Pre-time zero spectral vectors were averaged and subtracted from the whole data set to remove residual background pump scatter. The dispersion curve was fit to a third-order polynomial function to correct for the temporal chirp.

## S1.2. Synthetic Details



**Scheme S1.** Synthesis of *N,N*-dimethyl-3-oxo-3-phenylpropan-1-aminium chloride.

### *N,N*-dimethyl-3-oxo-3-phenylpropan-1-aminium chloride (Mannich reagent)

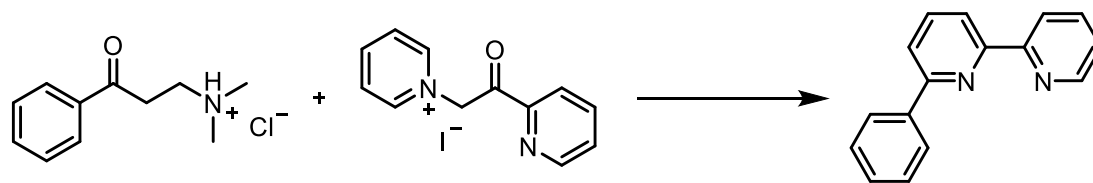
Literature procedure from ref 2 was followed. Dimethylamine hydrochloride (1.95 g; 1.3 eq), paraformaldehyde (0.74 g; 1.3 eq.) and acetophenone (2.15 mL; 18 mmol; 1 eq.) were suspended in 10 mL of ethanol. After addition of 0.5 mL conc. HCl the mixture heated under reflux for 22 h and then cooled to room temperature. The solution was diluted with 40 mL of acetone and kept at 4 °C (fridge) for 3 days. The white crystalline solid was then filtered off, washed with acetone and dried under vacuum (yield: 0.54 g). The second batch of crystalline solid was obtained by concentrating the filtrate under reduced pressure, addition of acetone, and keeping at 4 °C (yield: 1.03 g).

Yield: 1.57 g (40 %).

<sup>1</sup>H-NMR (CDCl<sub>3</sub>):  $\delta$  = 8.00 (d, 2H), 7.63 (t, 1H), 7.50 (t, 2H), 3.77 (t, 2H), 3.52 (t, 2H), 2.84 (s, 6H).

Characterization is consistent with previous report.<sup>2</sup>





**Scheme S2.** Synthesis of 6-phenyl-2,2'-bipyridine.

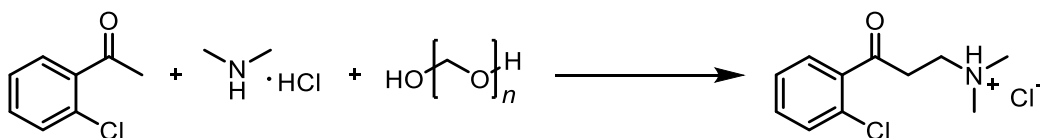
### 6-phenyl-2,2'-bipyridine

Literature procedure from ref 5 was followed. A suspension of 1-(2-oxo-2-(pyridin-2-yl)ethyl)pyridinium iodide (Kröhnke Reagent) (2.4 g; 7.4 mmol; 1 eq.) and 5.66 g ammonium acetate (10 eq.) in 18.3 mL of glacial acetic acid was refluxed for 20 min. After addition of *N,N*-dimethyl-3-oxo-3-phenylpropan-1-aminium chloride (Mannich reagent) (1.57 g; 1 eq.), the solution was heated under reflux for further 22 h. After cooling to room temperature the solvent was removed and the residue was diluted with 45 mL of chloroform and 45 mL of water, and the solids were filtered off. The organic phase was washed with water (45 mL) and saturated Na<sub>2</sub>CO<sub>3</sub> (45 mL). Chloroform was evaporated, yielding a dark brown oil, which was redissolved in small amount of DCM and passed through a silica plug using a mixture of EtOAc/hexanes (1/9) as an eluent. Solvents were removed under reduced pressure, yielding dark brown oil, which turned immediately into brown crystalline solid. The solid was washed with hexanes and dried on the Schlenk line.

Yield: 0.46 g (27 %).

<sup>1</sup>H-NMR (CDCl<sub>3</sub>): δ = 8.70 (m, 1H), 8.65 (m, 1H), 8.38 (dd, 1H), 8.16 (m, 2H), 7.92-7.84 (m, 2H), 7.78 (dd, 1H), 7.54-7.50 (m, 2H), 7.46-7.43 (m, 1H), 7.33 (m, 1H).

Characterization is consistent with previous report.<sup>5</sup>



**Scheme S3.** Synthesis of 3-(2-chlorophenyl)-*N,N*-dimethyl-3-oxopropan-1-aminium chloride.

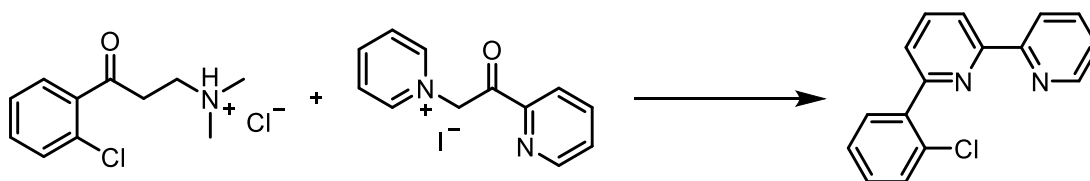
### 3-(2-chlorophenyl)-*N,N*-dimethyl-3-oxopropan-1-aminium chloride (Mannich reagent)

Literature procedure from ref 2 was followed. Dimethylamine hydrochloride (7.8 g; 1.3 eq.), paraformaldehyde (2.94 g; 1.3 eq.) and 2'-chloroacetophenone (9.55 mL; 74 mmol; 1 eq.) were suspended in 40 mL of ethanol. After addition of 2 mL conc. HCl the mixture heated under reflux for 22 h and then cooled to room temperature. The solution was diluted with 150 mL of acetone and kept at 4 °C (fridge) for 3 days. The white crystalline solid was then filtered off, washed with acetone and dried under vacuum (yield: 6.4 g). The second batch of crystalline solid was obtained by concentrating the filtrate under reduced pressure, addition of acetone, and keeping at 4 °C (yield: 2.15 g).

Yield: 8.55 g (54 %).

<sup>1</sup>H-NMR (CDCl<sub>3</sub>): δ = 7.62 (d, 1H), 7.45 (m, 2H), 7.38 (m, 1H), 3.74 (t, 2H), 3.49 (t, 2H), 2.85 (s, 6H).

Characterization is consistent with previous report.<sup>2</sup>



**Scheme S4.** Synthesis of 6-(2-chlorophenyl)-2,2'-bipyridine.

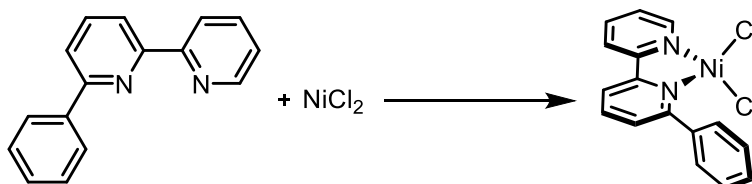
### 6-(2-chlorophenyl)-2,2'-bipyridine

Literature procedure from ref 2 was followed. A suspension of 1-(2-oxo-2-(pyridin-2-yl)ethyl)pyridinium iodide (Kroehnke Reagent) (5.25 g; 16 mmol; 1 eq.) and 12.36 g ammonium acetate (10 eq.) in 40 mL of glacial acetic acid was refluxed for 20 min. After addition of 3-(2-chlorophenyl)-*N,N*-dimethyl-3-oxopropan-1-aminium chloride (Mannich reagent) (3.98 g; 1 eq.), the solution was heated under reflux for further 22 h. After cooling to room temperature the solvent was removed and the residue was diluted with 100 mL of chloroform and 100 mL of water, and the solids were filtered off. The organic phase was washed with water (100 mL) and saturated  $\text{Na}_2\text{CO}_3$  (100 mL). Chloroform was evaporated, yielding a dark brown oil, which was redissolved in small amount of DCM and passed through a silica plug using a mixture of EtOAc/hexanes (1/9) as an eluent. Solvents were removed under reduced pressure, yielding dark brown oil, which turned immediately into brown crystalline solid. The solid was washed with hexanes and dried on the Schlenk line.

Yield: 2.19 g (51 %).

$^1\text{H-NMR}$  ( $\text{CDCl}_3$ ):  $\delta$  = 8.70 (m, 1H), 8.52 (m, 1H), 8.42 (dd, 1H), 7.90 (t, 1H), 7.81 (td, 1H), 7.73-7.68 (m, 2H), 7.51 (dd, 1H), 7.42-7.35 (m, 2H), 7.35-7.30 (m, 1H).

Characterization is consistent with previous report.<sup>2</sup>



**Scheme S5.** Synthesis of  $\text{Ni}(\text{PhBpy})\text{Cl}_2$

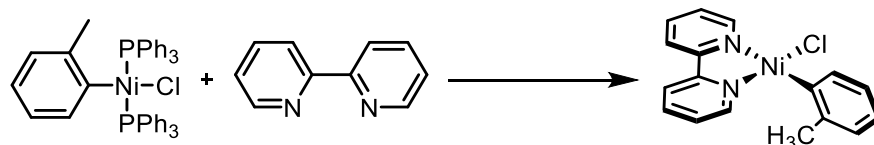
### $\text{Ni}(\text{PhBpy})\text{Cl}_2$

Literature procedure from ref 6 was followed. Under an inert atmosphere, 6-phenyl-2,2'-bipyridine (0.2 g; 0.86 mmol; 1 eq.) was dissolved in DCM (3 mL), added to  $\text{NiCl}_2$  (0.112 g; 1 eq.), and stirred at room temperature. Initial yellow color has changed to light green after ~24 hours. The reaction was kept stirring for total of 48 hours. The light green solid was then filtered off, washed with hexanes and dried under vacuum.

Yield: 93 mg (30 %).

$^1\text{H-NMR}$  ( $\text{D}_2\text{O}$ ):  $\delta$  = 55.1 (broad s), 50.0 (broad s), 41.9 (broad s), 16.6 (broad s). 9.4-8.5 (broad m).

UV-vis(water):  $\lambda_{\text{max}}$  = 303 nm.



**Scheme S6.** Synthesis of Ni(bpy)(CH<sub>3</sub>Ph)Cl.

### Ni(bpy)(CH<sub>3</sub>Ph)Cl, complex 1

Literature procedure from ref 1 was followed. Under an inert atmosphere, 2,2'-bipyridine (0.052 g, 0.33 mmol; 1 eq.) in diethyl ether (6 mL) was added to bis(triphenylphosphino)(2-methylphenyl)chloronickel(II) (0.263 g, 1 eq.). The red/orange mixture was stirred for 4 hours affording a bright red solid. The solid was filtered and washed with hexanes, diethyl ether, and pentane, and dried under vacuum.

Yield: 100 mg (88 %).

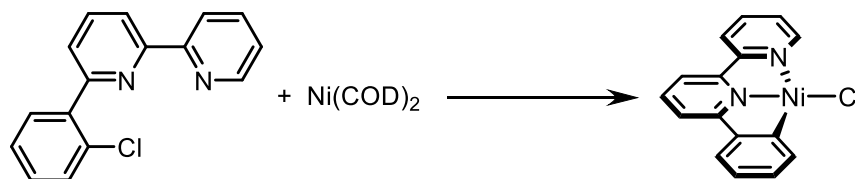
<sup>1</sup>H-NMR (CD<sub>2</sub>Cl<sub>2</sub>): δ = 9.22 (s, 1H), 8.02 (s, 1H), 7.96 – 7.86 (m, 5H), 7.54 (d, 2H), 7.33 (s, 1H), 7.13 (s, 1H), 6.81 (s, 3H), 3.04 (s, 3H).

<sup>13</sup>C{<sup>1</sup>H}-NMR: (CD<sub>2</sub>Cl<sub>2</sub>) δ = 156.3, 152.9, 151.9, 150.2, 149.8, 142.6, 139.2, 138.1, 135.77, 127.7, 126.9, 126.4, 123.4, 123.0, 121.2, 120.5, 25.1.

UV-vis(THF): λ<sub>max</sub> = 483 nm, ε<sub>483</sub> = 4070 M<sup>-1</sup> cm<sup>-1</sup>.

UV-vis(toluene): λ<sub>max</sub> = 502 nm, ε<sub>502</sub> = 1600 M<sup>-1</sup> cm<sup>-1</sup>.

Characterization is consistent with previous report.<sup>1</sup>



**Scheme S7.** Synthesis of Ni(PhBpy)Cl.

### Ni(PhBpy)Cl, complex 2

Literature procedure from ref 2 was followed. Under an inert atmosphere, the 6-(2-chlorophenyl)-2,2'-bipyridine (267 mg; 1 mmol; 1 eq.) was dissolved in 10 mL of dry THF and added to bis-(1,5-cyclooctadiene)nickel(0) (275 mg; 1 eq.). The reaction mixture turned dark red and was stirred at room temperature for 22 hours. Brick-red solid was filtered and washed with pentane, and dried under vacuum.

Yield: 0.283 g (87 %).

<sup>1</sup>H-NMR (CD<sub>2</sub>Cl<sub>2</sub>): δ = 8.97 (d, 1H), 8.00 (m, 1H), 7.89-7.83 (m, 2H), 7.55 (m, 1H), 7.52-7.48 (m, 3H), 7.30 (m, 1H), 7.06 (m, 2H).

<sup>13</sup>C{<sup>1</sup>H}-NMR: (CD<sub>2</sub>Cl<sub>2</sub>) δ = 164.6, 154.3, 154.3, 150.7, 148.8, 147.5, 139.9, 139.9, 138.9, 129.9, 126.8, 125.5, 122.6, 120.8, 118.5, 117.5.

μ<sub>eff</sub> = 0.7 μ<sub>B</sub> (Evans method, 298 K, CD<sub>2</sub>Cl<sub>2</sub>).

UV-vis(THF): λ<sub>max</sub> = 507 nm, ε<sub>507</sub> = 2802 M<sup>-1</sup> cm<sup>-1</sup>.

UV-vis(toluene): λ<sub>max</sub> = 521 nm, ε<sub>521</sub> = 2267 M<sup>-1</sup> cm<sup>-1</sup>.

Characterization is consistent with previous report.<sup>2</sup>

Evans method for complex **2** in  $\text{CD}_2\text{Cl}_2$  with 2-MeTHF internal standard

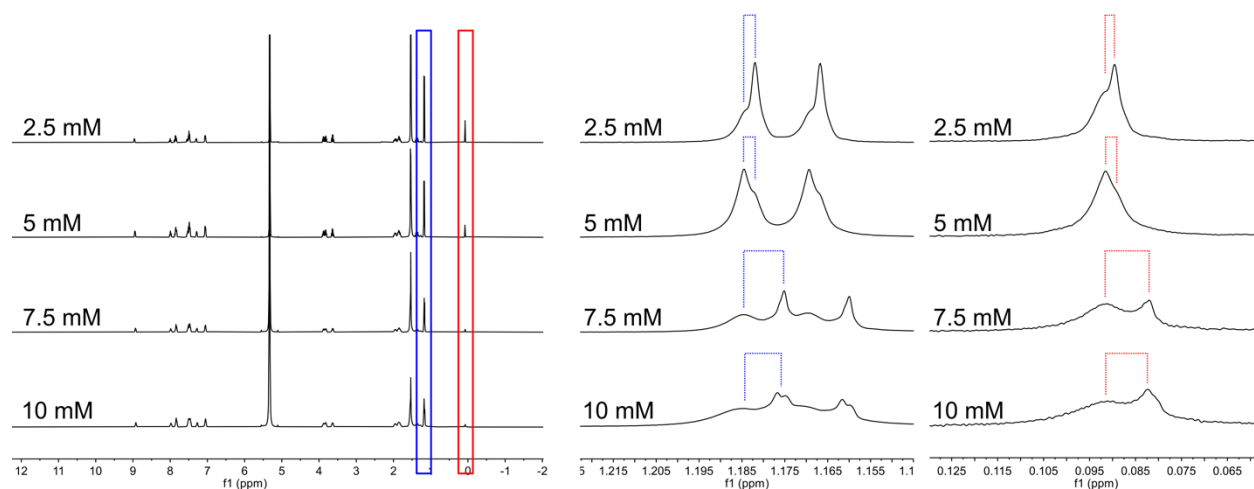
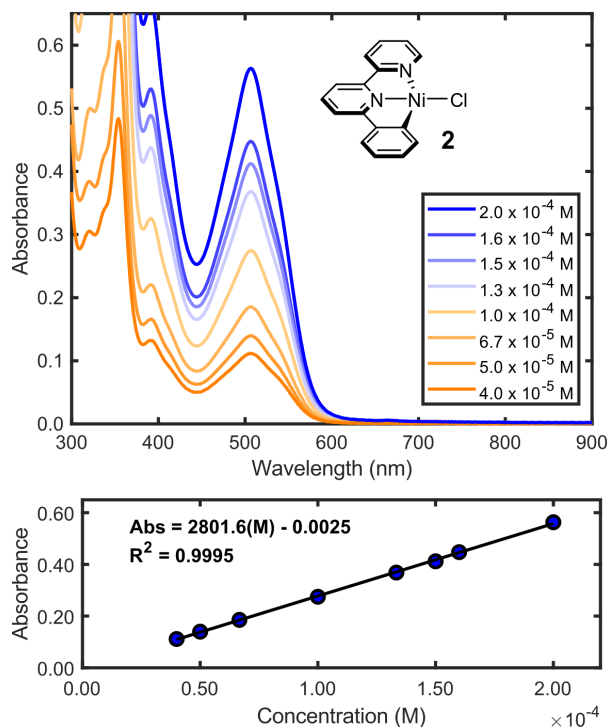


**Figure S1.** Evans method:  $^1\text{H}$ -NMR (400 MHz,  $\text{CD}_2\text{Cl}_2$ ) spectrum of complex **2** with 2-MeTHF as an internal standard.

The effective magnetic moment ( $\mu_{\text{eff}}$ ) of **2** ( $0.7 \mu_{\text{B}}$ ) deviates from the expected value of zero for a diamagnetic compound with a singlet electronic ground state. We attribute this non-zero value to the presence of a paramagnetic impurity. Since the synthesis of **2** involves an intramolecular oxidative addition of the aryl halide tethered to the bpy ligand (**Scheme S7**), which eliminates the need for excess aryl halide, the impurity could potentially arise from a Ni disproportionation process during the synthesis or  $\text{Ni}(\text{COD})_2$  decomposition. A  $\mu_{\text{eff}}$  of  $0.7 \mu_{\text{B}}$  corresponds to  $\sim 0.2$  unpaired electrons in the sample, which falls below an integer number. Nevertheless, the concentration of paramagnetic impurity can be estimated by analyzing the chemical shifts observed in the Evans method (**Figure S1**). For a triplet (two unpaired electrons), the expected  $\mu_{\text{eff}}$  is  $\sqrt{8} \mu_{\text{B}}$ . This allows us to assess the concentration of a triplet species and compare to the concentrations of individually prepared samples in **Figure S1**. By this, a triplet impurity would constitute  $\sim 6\%$  of the total sample mass. Similarly, if we were to consider the presence of a less likely doublet impurity, its estimated concentration would be  $\sim 17\%$ . We also note that the concentration of Ni in the Evans method experiments is  $\sim$ two orders of magnitude higher than a typical photochemical experiment conducted in this work. Significantly higher concentrations could result in sample aggregation, which could also potentially influence the measured  $\mu_{\text{eff}}$ .

### S1.3. Steady-State UV-vis Spectroscopy

a) Concentration-dependent UV-vis of **2** in THF



b) Concentration-dependent UV-vis of **2** in Toluene

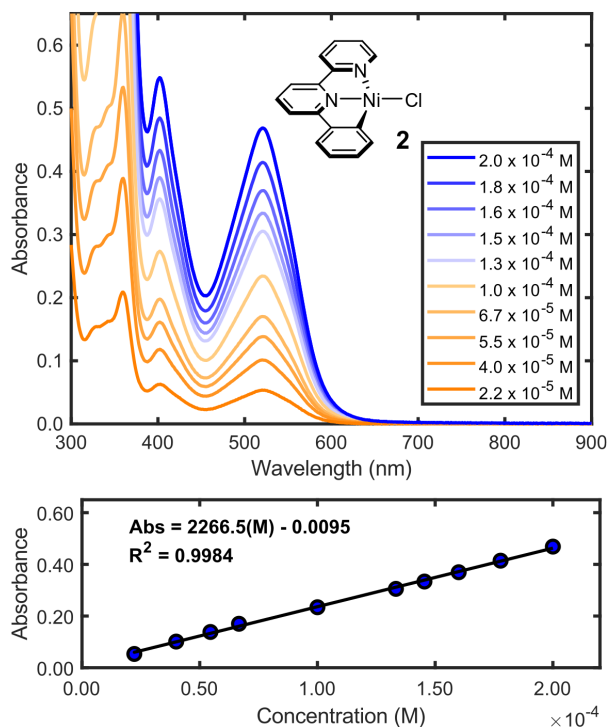


**Figure S2.** Concentration dependent UV-vis absorption spectra of complex **2**. a) in THF, b) in toluene.

Steady-state UV-vis absorption of **1** and **2** upon addition of 1000 eq. of mesityl bromide

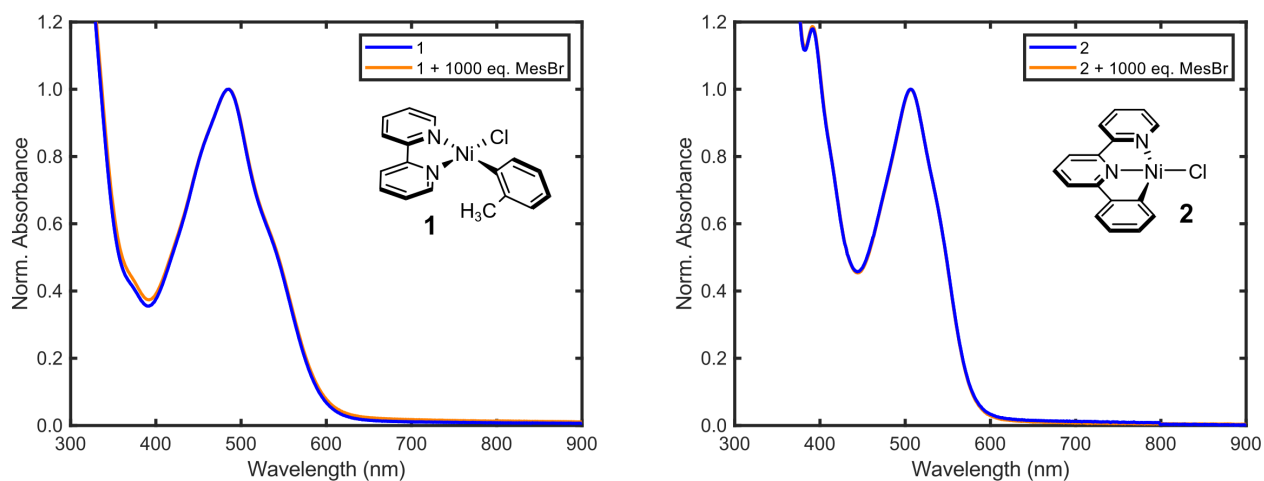


**Figure S3.** Change in the UV-vis absorption spectra of complexes **1** and **2** in THF upon addition of 1000 eq. of mesityl bromide

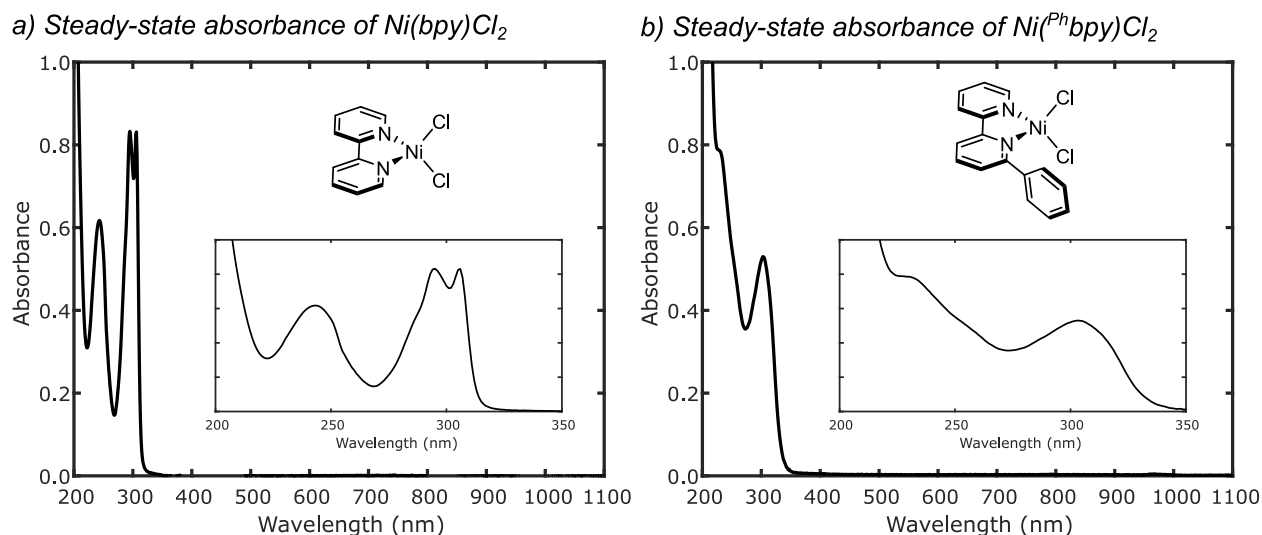


**Figure S4.** UV-vis absorption spectra in water of a)  $\text{Ni}(\text{bpy})\text{Cl}_2$  and b) synthesized  $\text{Ni}(\text{Phbpy})\text{Cl}_2$ .

## S1.4. Photolysis Experiments

### *Wavelength-Dependent Investigations*

We have conducted wavelength dependence analysis on complexes **1** and **2**. Employing a standard protocol, the samples were prepared in the glovebox using THF as a solvent, and distributed into air-tight seal cuvettes, which were positioned at a distance of  $\sim 5$  cm from the Kessil PR160L LED light sources (incident light:  $\lambda_{\text{max}} = 370$  nm, 390 nm, 427 nm, 456 nm, and 525 nm) on maximum intensity. The power of each LED was quantified using a Thorlabs S425C thermal detector power meter as follows: 370 nm ( $100 \text{ mW cm}^{-2}$ ), 390 nm ( $170 \text{ mW cm}^{-2}$ ), 427 nm ( $220 \text{ mW cm}^{-2}$ ), 456 nm ( $220 \text{ mW cm}^{-2}$ ), and 525 nm ( $100 \text{ mW cm}^{-2}$ ).

Considering complex **1**, a noticeable diminution in quantum yields was observed in tandem with the decrease in incident-light energy. No photolysis was observed when complex **1** was irradiated with 525 nm LED (**Figure S5**). In contrast, there was no photolysis observed for **2** after 1 hour of irradiation irrespective of the wavelength employed (**Figure S6**).

Photoirradiation of **1** in THF using various LEDs

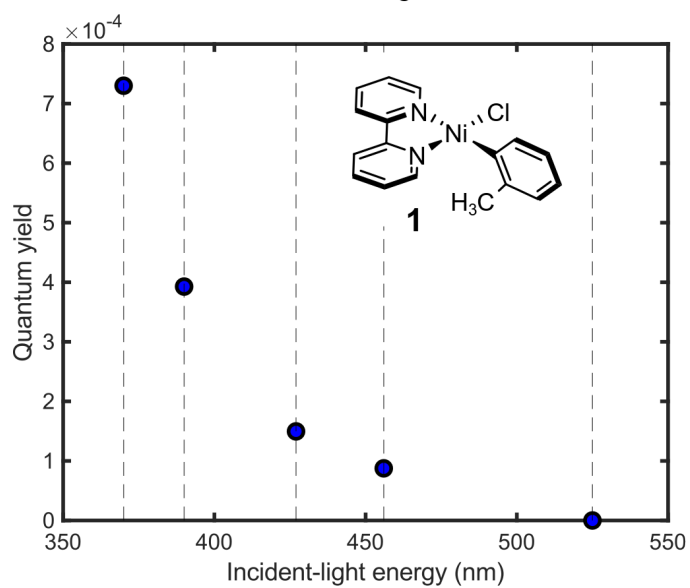
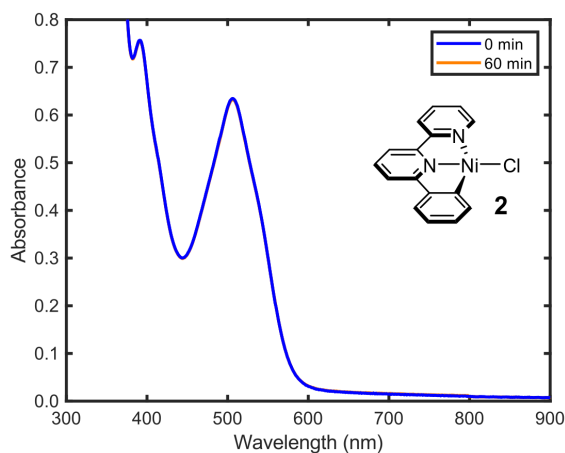
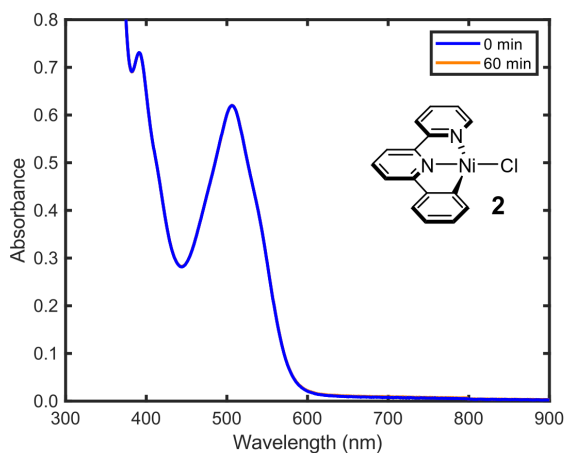


**Figure S5.** Quantum yields of photochemical Ni–C bond homolysis of complex **1** using different incident-light wavelengths. Note that quantum yields for irradiation of **1** at 370 nm and 390 nm were reported previously in ref 7 and ref 1, respectively.

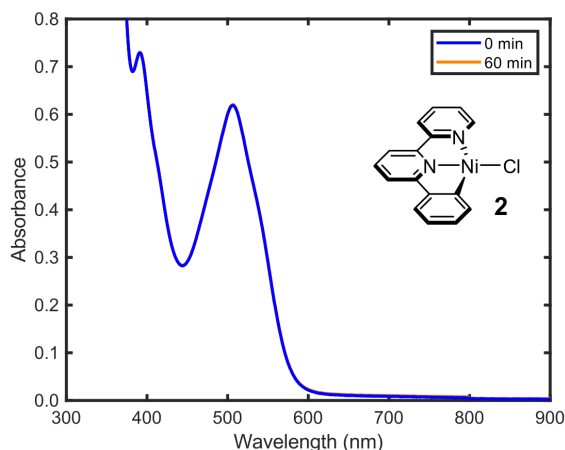
a) Photoirradiation of **2** in THF using 370 nm LED



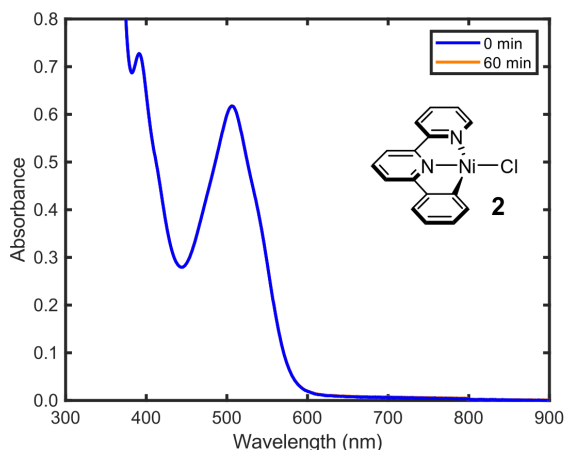
b) Photoirradiation of **2** in THF using 427 nm LED



c) Photoirradiation of **2** in THF using 456 nm LED



d) Photoirradiation of **2** in THF using 525 nm LED

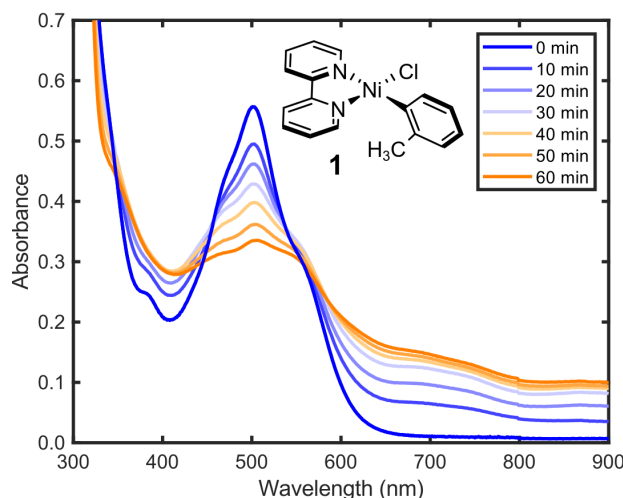
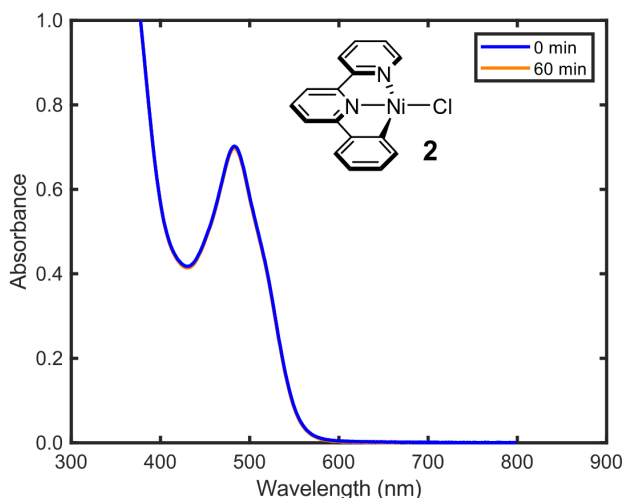


**Figure S6.** Irradiation of complex **2** using different incident-light wavelengths, a) 370 nm, b) 427 nm, c) 456 nm, d) 525 nm. Plotted are the UV-vis absorption spectra at  $t = 0$  min and  $t = 60$  min. Note that irradiation at 390 nm is reported in **Figure 3** in the main text.

### Solvent-Dependent Investigations

Besides photochemical experiments performed in THF, we have also irradiated complexes **1** and **2** in toluene (**Figure S7**), using the same photochemical setup (Kessil PR160L LED with  $\lambda_{\text{max}} = 390$  nm and the LED power of  $170 \text{ mW cm}^{-2}$ ).



a) Photoirradiation of **1** in tolueneb) Photoirradiation of **2** in toluene

**Figure S7.** Photoirradiation of complexes **1** and **2** in toluene using 390 nm LED. a) complex **1**, b) complex **2**.

In summary, our observations reveal that complex **1** exhibits the anticipated photochemical behavior, aligning with previously documented findings related to the threshold incident-energy wavelength,<sup>1,8</sup> and the rate of Ni–C bond homolysis that is wavelength dependent.<sup>1</sup> Conversely, complex **2** showcases chemical and photochemical stability in solution across a spectrum of LED wavelengths. The stability of complex **2** furthermore extends to both coordinating (THF) and non-coordinating solvents (toluene). This similarity suggests that the equilibrium governing the reversible Ni–C bond homolysis is not influenced by the choice of the solvent. We also note that complex **2** undergoes decomposition in DMF, a strongly coordinating solvent. This event is likely triggered by the displacement of the bpy ligand, a phenomenon previously expounded upon in refs 9,10 regarding Ni–(bpy) aryl halide complexes.

### Radical Trapping Monitored by Electron Paramagnetic Resonance

To detect potential ejected radicals from **1** and **2**, we have performed spin-trapping experiments, employing a 9-Azabicyclo[3.3.1]nonane *N*-Oxyl (ABNO) radical trap and continuous wave (CW) EPR. First, we have performed a control experiment by dissolving the ABNO radical trap in toluene (14 mM) in a nitrogen-filled glovebox and collecting a room-temperature CW EPR spectrum. This resulted in a signal characteristic of the ABNO radical trap. An aliquot of the same stock solution was then irradiated in a 2-mm air-free UV-vis cuvette with 390 nm LED for 1 hour. The CW EPR spectrum recorded after irradiation indicated that no radical trap was consumed in the absence of either complex **1** or **2** (**Figure S8a**). However, irradiation in the presence of the untethered complex Ni(II)–<sup>4,4'</sup>-tBu<sub>2</sub>bpy *o*-tolyl bromide, which is similar to **1** and has been utilized due to the insufficient solubility of **1** in toluene, resulted in the consumption of radical trap as evidenced by the decreased EPR signal (**Figure S8b**). This result for the untethered compound is consistent with a previous report.<sup>11</sup> In contrast to **1**, tethered complex **2** does not exhibit decreased radical trap EPR signal upon irradiation, supporting the absence of appreciable amounts of dissociated, out-of-cage radical formation (**Figure S8c**). The result for **2** is also consistent with the reversible Ni(II)–C bond activation mechanism proposed herein for **2**.

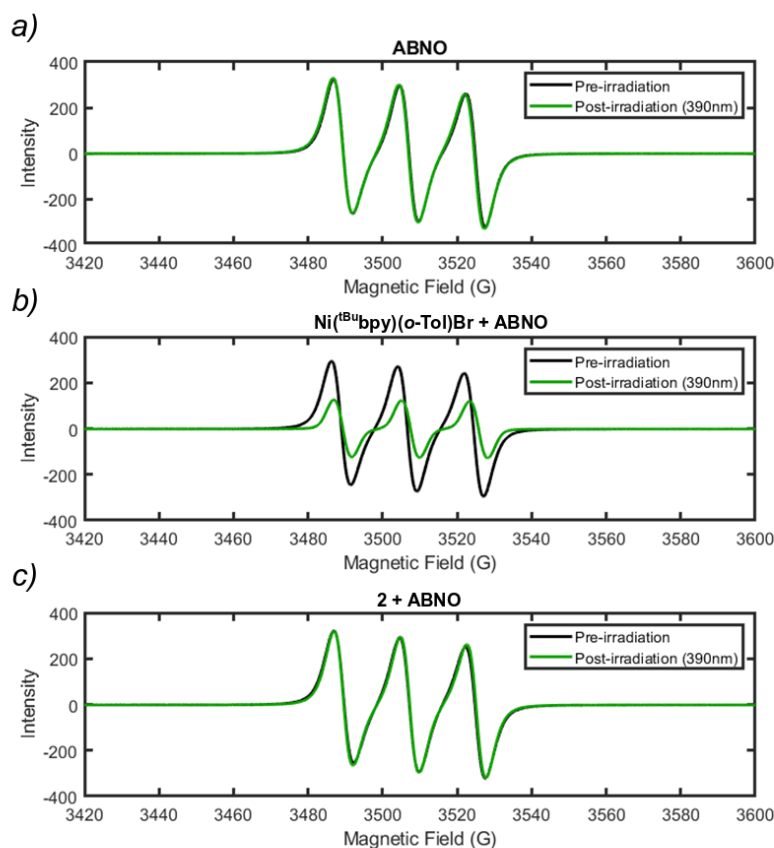
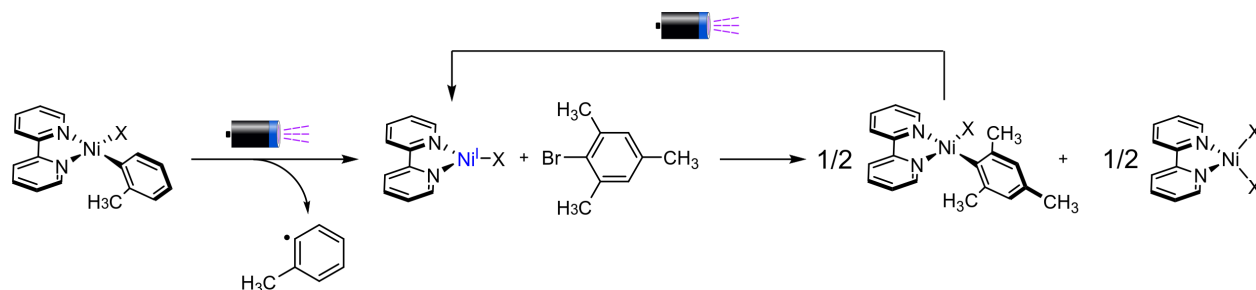


**Figure S8.** Room-temperature CW EPR spectra of ABNO radical trap in toluene before (black trace) and after (green trace) irradiation with 390 nm LED. a) in the absence of **1** and **2**, b) with 1 eq. of Ni(II)–4,4′-tBu<sub>2</sub>bpy *o*-tolyl bromide, c) with 1 eq. of **2**.

### ***Irradiation with Mesityl Bromide Additive***

Upon subjecting complex **1** to irradiation in the presence of mesityl bromide, a notable and effective suppression of the ensuing Ni(I) intermediate is observed, in line with the proposed mechanism delineated in **Scheme S8**. Akin to findings in ref 7, a large excess of aryl halide is necessary for an efficient oxidative addition reactivity. Computational insights from previous DFT studies revealed that Ni(I)–bpy chloride derived from the photochemical reactivity of **1** engages with tolyl bromide with a relatively large free energy barrier of  $\sim 17.1$  kcal mol<sup>-1</sup>. Furthermore, it is anticipated that the oxidative addition reactivity would be even more challenging for the sterically encumbered mesityl bromide. This is observed experimentally in this work, where the full suppression of the characteristic Ni(I) absorption feature is achieved only in the presence of a significant excess of mesityl bromide, with approximately 100 equivalents proving necessary (**Figure S9**).



**Scheme S8.** Proposed photochemical reactivity of **1** in the presence of mesityl bromide. The photochemically produced Ni(I)-bpy halide intermediate reacts with mesityl bromide to yield new Ni(II)-bpy mesityl halide and Ni(II)-bpy dihalide in 1:1 ratio. The Ni(II)-bpy mesityl halide would also be photochemically active, producing the same Ni(I)-bpy halide intermediate. Ultimately, irradiation of the reaction mixture thus leads to an accumulation of sparingly soluble Ni(II)-bpy dihalide.

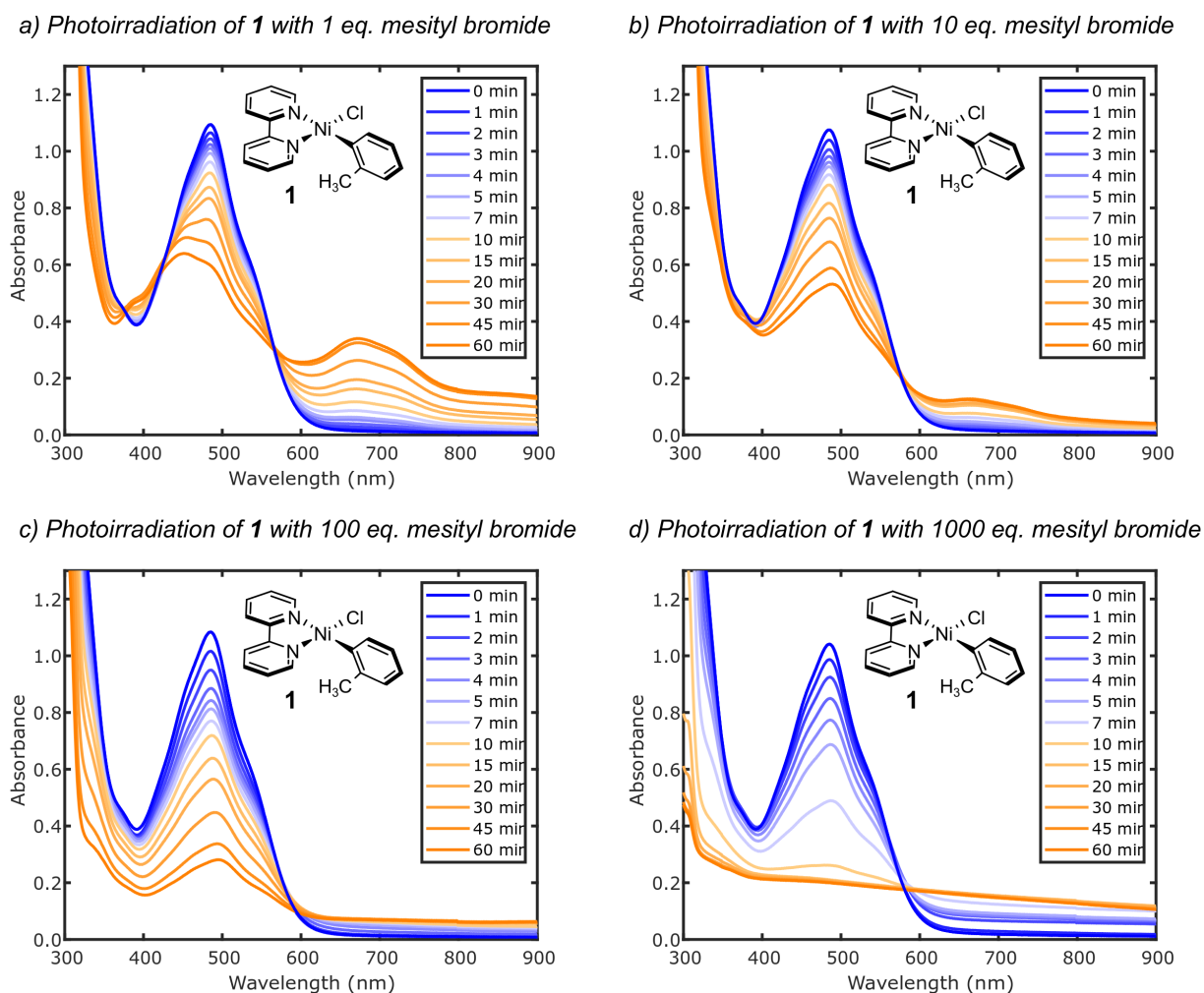


**Figure S9.** Irradiation of **1** in THF using 390 nm LED with varied concentration of mesityl bromide. a) 1 eq. mesityl bromide, b) 10 eq. mesityl bromide, c) 100 eq. mesityl bromide, d) 1000 eq. mesityl bromide.

A different behavior was observed for irradiation of complex **2** with mesityl bromide. The reversibility inherent in the photochemical activation of the Ni(II)–C bond translates to slower reactivity when exposed to low concentrations of mesityl bromide. However, with higher concentration (above ~100 eq. excess) of mesityl bromide, a productive decay of the Ni(II) absorption features becomes evident. Particularly noteworthy, when subjecting complex **2** to 1000 eq. excess of mesityl bromide, a new species is formed that is distinguishable with an absorbance peak at  $\lambda_{\text{max}} = 555$  nm.

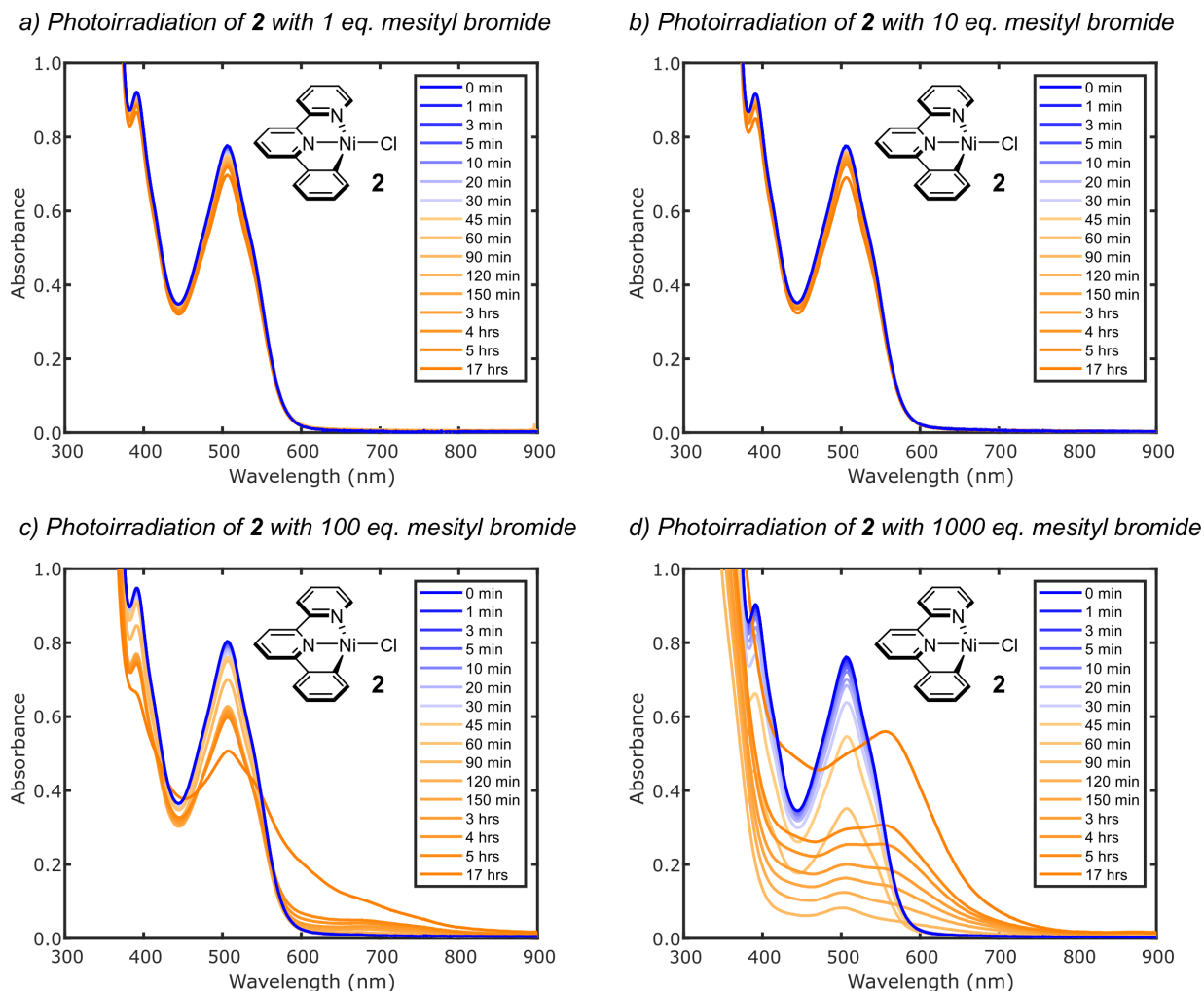
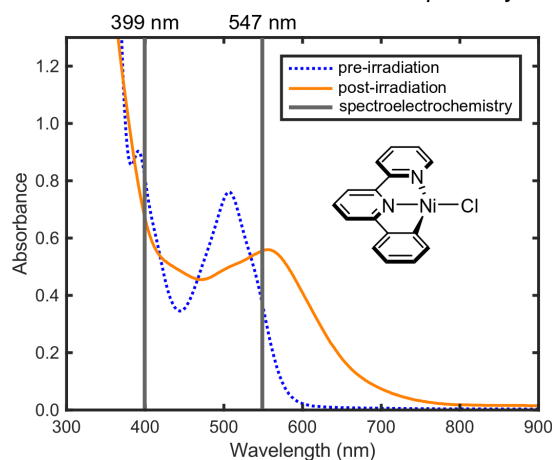


**Figure S10.** Irradiation of **2** in THF using 390 nm LED with varied concentration of mesityl bromide. a) 1 eq. mesityl bromide, b) 10 eq. mesityl bromide, c) 100 eq. mesityl bromide, d) 1000 eq. mesityl bromide.

We have sought to understand the nature and stability of the product of irradiation of **2** in the presence of high concentrations of mesityl bromide. Upon prolonged irradiation, a distinctive species emerges, characterized by an absorption peak at  $\lambda_{\text{max}} = 555$  nm. Based on the comparison of the UV-vis spectra with the spectroelectrochemical data from ref 5 (**Figure S11**), we attribute this newly formed species as a tethered Ni(I)–bpy phenyl intermediate.

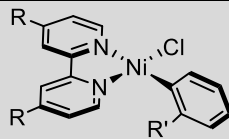
Notably, the absorption signature resides at a substantially higher energy than the corresponding absorption band attributed to the Ni(I)–bpy halide intermediate originating from irradiation of untethered Ni(II)–bpy aryl halide complexes, including **1** (Table S1).<sup>1</sup> All previously characterized Ni(I)–bpy halides exhibit significantly greater red-shifts ( $\sim 5900\text{ cm}^{-1}$  on average) relative to the intermediate observed herein ( $\sim 1700\text{ cm}^{-1}$ ), supporting a tethered Ni(I)–bpy phenyl and not the Ni(I)–bpy halide at the end of photoirradiation with large excess electrophile. Following this characterization, we have computed the UV-vis spectra of tridentate, tethered Ni(I)–bpy phenyl and Ni(I)–<sup>Ph</sup>bpy chloride intermediates using the spin-orbit corrected CASSCF/QD-NEVPT2 level of theory (Figure S31). The spectrum of Ni(I)–<sup>Ph</sup>bpy chloride is red-shifted relative to the Ni(I)–bpy phenyl complex. The more significant red shift for the halide complex contrasts the experimental observation and corroborates assignment to the tethered Ni(I)–bpy phenyl species

Photoirradiation of **2** with addition of 1000 eq. mesityl bromide



**Figure S11.** Comparison of the absorption spectrum resulting from a prolonged irradiation of **2** with 1000 eq. of mesityl bromide, and the peak maxima from reductive spectroelectrochemistry of tethered Ni(II)-bpy aryl bromide complex from ref. 5. It should be noted that spectroelectrochemical analysis was performed in THF/*n*Bu<sub>4</sub>NPF<sub>6</sub> solutions, while our spectra are obtained in THF without electrolyte. This difference may result in small shifts in the peaks positions.

**Table S1.** Comparison of the absorption maxima of Ni(II) and Ni(I) states from ref 1 and complexes **1** and **2** in this work.

		Ni(II) $\lambda_{i,max}$ (nm / $\text{cm}^{-1}$ )	Ni(I) $\lambda_{i,max}$ (nm / $\text{cm}^{-1}$ )	Ni(II) vs. Ni(I) $\lambda_{i,max}$ difference, $\Delta$ (nm / $\text{cm}^{-1}$ )
R = OMe	R' = Me	462 / 21 600	577 / 17 300	115 / 4 300
t-Bu	Me	475 / 21 100	657 / 15 200	182 / 5 900
COOMe	Me	532 / 18 800	807 / 12 400	275 / 6 400
t-Bu	H	471 / 21 200	662 / 15 100	191 / 6 100
t-Bu	OMe	464 / 21 600	657 / 15 200	193 / 6 400
t-Bu	F	447 / 22 400	652 / 15 300	205 / 7 100
OMe	CF <sub>3</sub>	432 / 23 100	547 / 18 300	115 / 4 800
H	CF <sub>3</sub>	453 / 22 100	568 / 17 600	115 / 4 500
COOMe	CF <sub>3</sub>	497 / 20 100	800 / 12 500	303 / 7 600
Average $\Delta$ : 5 900 $\text{cm}^{-1}$				

<b>1</b>	485 / 20 600	670 / 14 900	187 / 5 700
<b>2</b>	507 / 19 700	555 / 18 000	48 / 1 700

To further characterize the species, we have also performed continuous-wave electron paramagnetic resonance (CW-EPR) measurements. We subjected a sample to irradiation in the presence of a 1000-fold excess of mesityl bromide in 2-MeTHF and subsequently froze it in liquid nitrogen. While room-temperature UV-vis data exhibited an identical electronic absorption spectrum as that observed in THF, no resolvable EPR signals were obtained even at 5 K temperature in both perpendicular and parallel EPR modes. In contrast, room-temperature paramagnetic  $^1\text{H}$ -NMR gave signals that hint a mixture of various species, likely including Ni(I)–bpy aryl, Ni(I)–bpy halide, and Ni(II)–bpy dihalide (**Figure S12**).

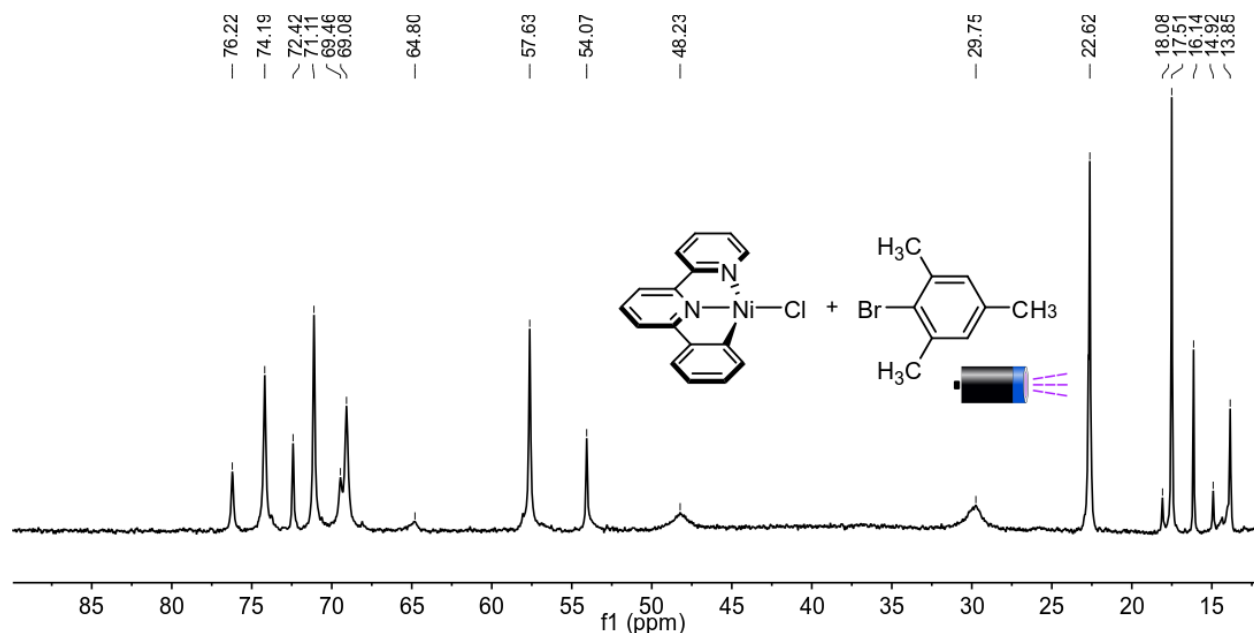
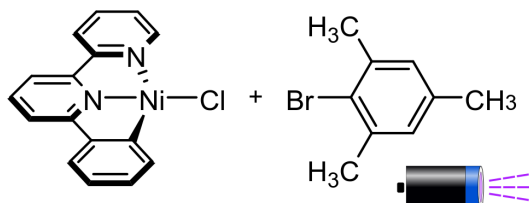


**Figure S12.** Paramagnetic region of  $^1\text{H}$ -NMR.

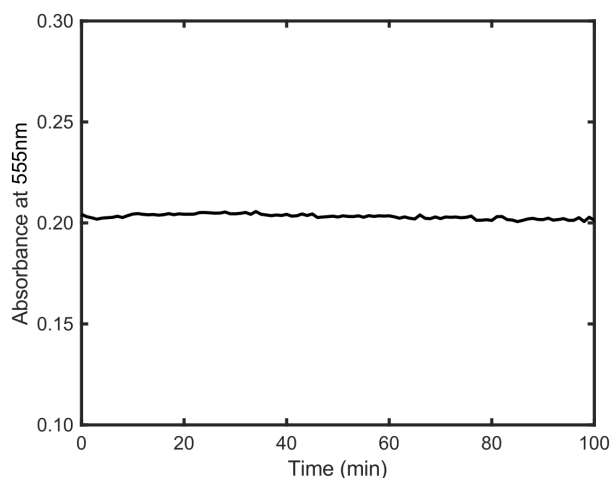
We have further probed the stability of the product by conducting a time-dependent UV-vis absorption measurements at an elevated temperature of 50 °C. In light of prior findings indicating the dimerization propensity of Ni(I)–bpy halides under analogous experimental conditions, giving rise to  $[\text{Ni(I)–bpy halide}]_2$ ,<sup>7</sup> we sought to discern the fate of the photoproduct. Illustrated in **Figure S13a**, the absorbance at 555 nm is plotted over time, revealing no decay. This is indicative of no thermal decomposition of the product similar to the dimerization pathway observed for other Ni(I)–bpy halide species. The Ni(I)–bpy halides also showcase complex speciation responses upon freezing and/or concentrating, likely from a mixture of Ni(I)/Ni(I) and Ni(II)/Ni(I) dimers. For the photoproduct of complex **2** investigated herein, we note that it is amenable to concentration through solvent removal under vacuum and redissolution in THF, as it retains the same electronic absorption spectrum (**Figure S13b**). This scenario suggests either the absence of the equilibrium, potentially due to steric hindrance stemming from the tethered aryl ligand, or a complete reversibility of the equilibrium. Finally, we note that the photoproduct reacts quickly upon exposure to air (**Figure S13c**). Introducing air into the air-tight cuvette leads to a clear

decomposition of the compound. This particular reactivity echoes the behavior often observed with other Ni(I) and Ni(0) intermediates.

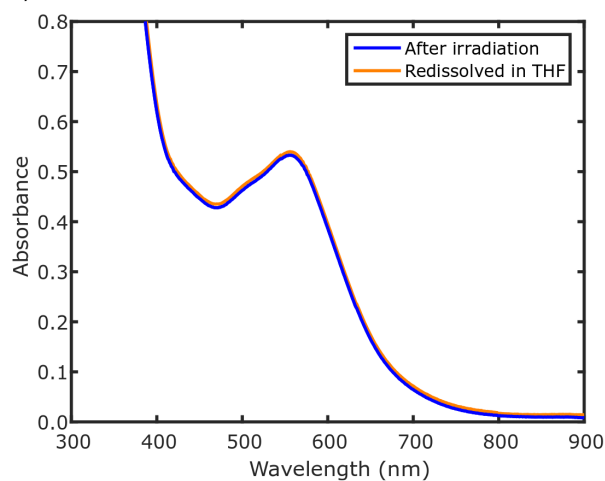
**Investigating the stability of the photoproduct of **2** + 1000 eq. mesityl bromide irradiation**



**a) Product decomposition at 50 °C**



**b) Product redissolution in THF**



**c) Product reacting with air**

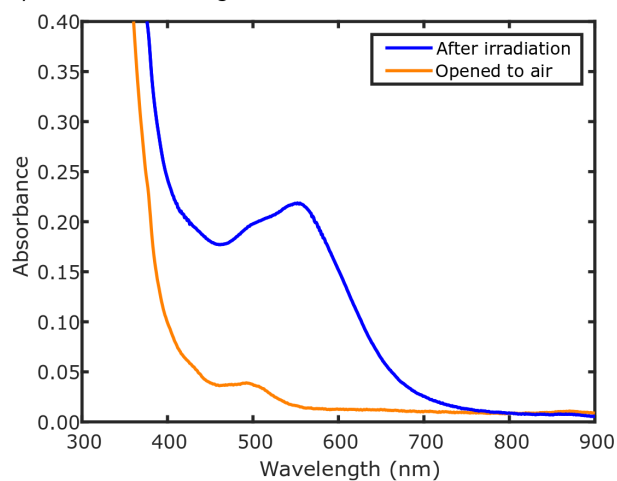


**Figure S13.** Stability and characterization of the product obtained from irradiating complex **2** with 1000 eq. excess of mesityl bromide in THF. a) heating at 50 °C, b) concentrating solution under vacuum and re-dissolving in THF, c) reactivity with air.

Motivated by the intriguing possibility to concentrate the solution of the photoproduct, we have attempted to crystallize the species for a single-crystal analysis. However, all of the attempts were unsuccessful, possibly due to the presence of a complex mixture of species in the solution, spanning from the unreacted Ni(II)–bpy aryl halide, Ni(II)–bpy dihalide, excess of mesityl bromide, and the target photoproduct. However, we were able to isolate a sparingly soluble light-green precipitate. Redissolving it in water and D<sub>2</sub>O, we have conducted UV-vis and paramagnetic <sup>1</sup>H-NMR measurements. These efforts enabled us to assign the species as Ni(II)–<sup>Ph</sup>bpy dihalide through a comparison with an independently synthesized compound (**Figure 4** in the main text).



### *Irradiations with Other Aryl Bromide Additives*

To shed light on the Ni(II) conversion and elucidate the electronic and steric effects of the substrates, we have performed irradiations of **2** with a variety of substituted aryl bromides and collected the time-dependent absorption spectra. Due to the complicated kinetics (see **Section S1.5**), only the extent of conversion of the Ni(II) starting material after 30 minutes of irradiation is used for comparison among aryl bromide substrates. These experiments demonstrate a pronounced electronic influence on the Ni(II) activation, with a trend of more electron-donating substituents contributing to the increased rate of aryl bromide activation (i.e., with 4-bromo-*N,N*-dimethylaniline as compared to 4-bromotoluene and 4-fluorobromobenzene). Steric effects are also seen, but without an obvious trend. Sterically encumbered mesityl bromide converts photoactivated **2** with greater ease than 2-bromotoluene, but the sterically accessible 4-bromotoluene is more active than 2-bromotoluene. We note that in the case of mesityl bromide, the steric effect may be dominated by the electronic enhancement mentioned above. Interestingly, these trends are unlike to what would be expected for aryl halide activation through a concerted oxidative addition mechanism.<sup>7,12,13</sup>

Photoirradiation of **2** with addition of 1000 eq. mesityl bromide

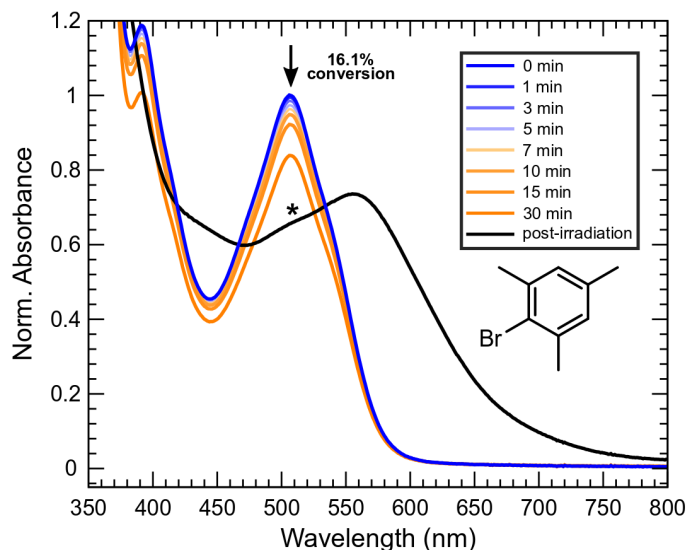


**Figure S14.** Irradiation of **2** in THF using 390 nm LED with 1000 eq. of mesityl bromide. The asterisk denotes residual signal likely corresponding to either remaining starting material or a secondary decomposition product (see **Figure S13c**). Due to the complicated kinetics (see **Section S1.5**), only the extent of conversion of the Ni(II) starting material after 30 minutes of irradiation (16.1%), obtained from the change in absorbance at 507 nm, is used for comparison to other aryl bromide substrates.



Photoirradiation of **2** with addition of 1000 eq. 4-bromo-*N,N*-dimethylaniline

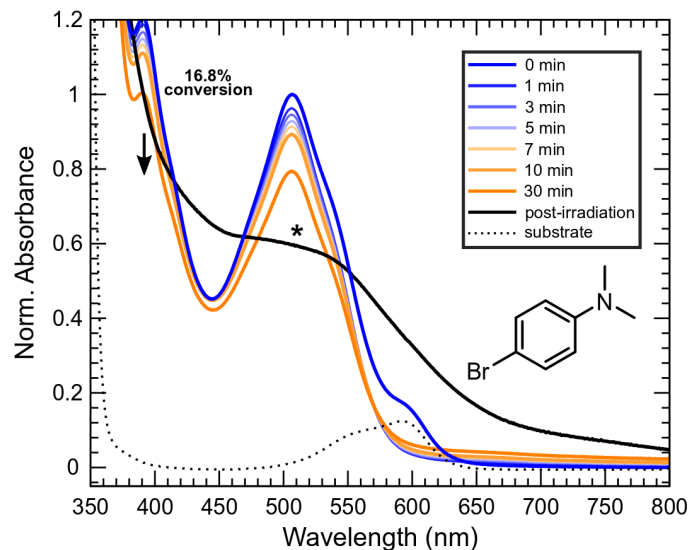


**Figure S15.** Irradiation of **2** in THF using 390 nm LED with 1000 eq. of 4-bromo-*N,N*-dimethylaniline. The asterisk denotes residual signal likely corresponding to either remaining starting material or a secondary decomposition product (see **Figure S13c**). Due to the complicated kinetics (see **Section S1.5**), only the extent of conversion of the Ni(II) starting material after 30 minutes of irradiation (16.8%), obtained from the change in absorbance at 391 nm (peak *ii*), is used for comparison to other aryl bromide substrates. Note that different wavelength was used due to spectral overlap of **2** and the substrate in the region of 507 nm (peak *i*).

Photoirradiation of **2** with addition of 1000 eq. 4-bromotoluene

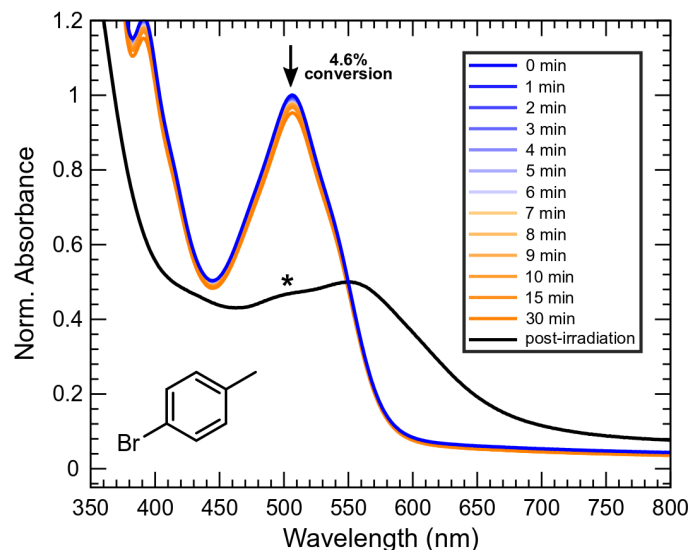


**Figure S16.** Irradiation of **2** in THF using 390 nm LED with 1000 eq. of 4-bromotoluene. The asterisk denotes residual signal likely corresponding to either remaining starting material or a secondary decomposition product (see **Figure S13c**). Due to the complicated kinetics (see **Section S1.5**), only the extent of conversion of the Ni(II) starting material after 30 minutes of irradiation (4.6%), obtained from the change in absorbance at 507 nm, is used for comparison to other aryl bromide substrates.

Photoirradiation of **2** with addition of 1000 eq. 2-bromotoluene

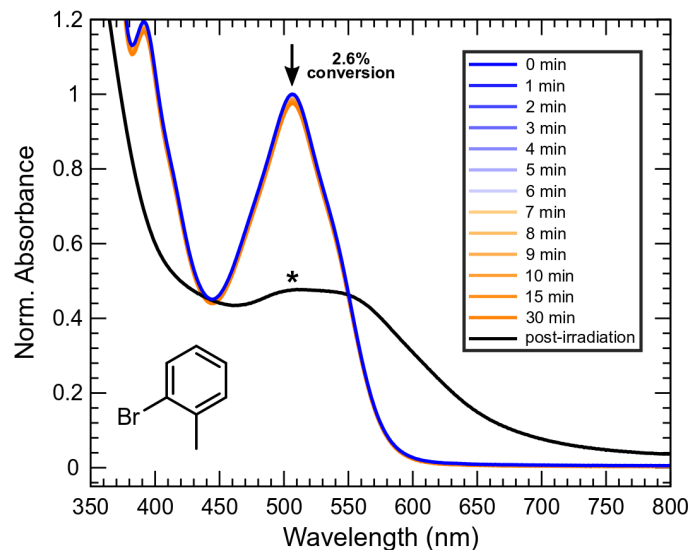


**Figure S17.** Irradiation of **2** in THF using 390 nm LED with 1000 eq. of 2-bromotoluene. The asterisk denotes residual signal likely corresponding to either remaining starting material or a secondary decomposition product (see **Figure S13c**). Due to the complicated kinetics (see **Section S1.5**), only the extent of conversion of the Ni(II) starting material after 30 minutes of irradiation (2.6%), obtained from the change in absorbance at 507 nm, is used for comparison to other aryl bromide substrates.

Photoirradiation of **2** with addition of 1000 eq. 4-fluorobromobenzene

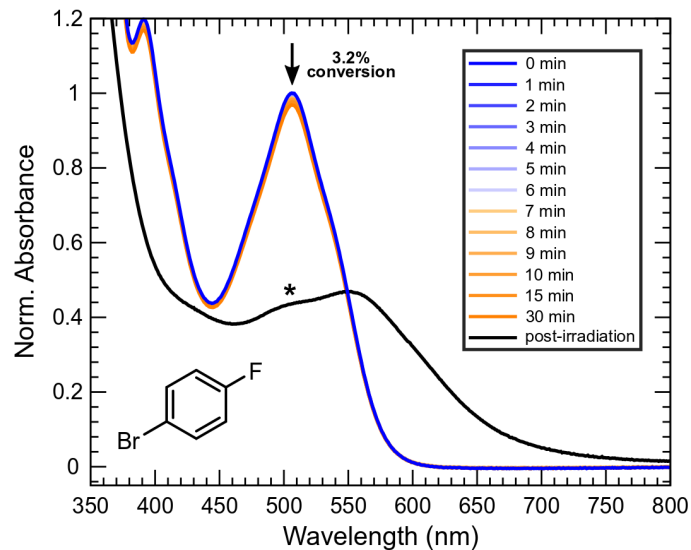


**Figure S18.** Irradiation of **2** in THF using 390 nm LED with 1000 eq. of 4-fluorobromobenzene. The asterisk denotes residual signal likely corresponding to either remaining starting material or a secondary decomposition product (see **Figure S13c**). Due to the complicated kinetics (see **Section S1.5**), only the extent of conversion of the Ni(II) starting material after 30 minutes of irradiation (3.2%), obtained from the change in absorbance at 507 nm, is used for comparison to other aryl bromide substrates.

### S1.5. Kinetic Modeling

In order to understand the influence of the addition of mesityl bromide on the photochemical reactivity of **1** and **2**, we have extracted the rate constants from time-resolved UV-vis absorption studies. Since the single-exponential fits contain the overlapping features of the starting material and the product of photolysis and also cannot account for the subsequent reactivity, e.g., photoproduct Ni(I) dimerization, we have attempted to decompose the spectral data using global kinetics modeling. Herein, we have evaluated a variety of kinetic models, starting from the two absorbing species (A, B) with a third species (C) with no absorbance over the investigated range (i.e., the model that was successfully employed previously for a kinetic analysis of **1** without the addition of mesityl bromide).<sup>1,7</sup> This set comprises the kinetic models, such as:  $[A \rightarrow B]$ ,  $[2A \rightarrow B]$ ,  $[A \rightarrow B, A \rightarrow C]$ ,  $[A \rightarrow B, B \rightarrow C]$ ,  $[A \rightarrow B, 2B \rightarrow C]$ ,  $[A \rightarrow C, C \rightarrow B]$ ,  $[A \rightarrow C, 2C \rightarrow B]$ .

For **1** with a low concentration of mesityl bromide, the models of  $[A \rightarrow B, 2B \rightarrow C]$  and  $[A \rightarrow B, B \rightarrow C]$  performed the best based on the root-mean-square of the residual absorbance matrix (RMSR), with the rate constants of  $k_p (A \rightarrow B) = 3.1 \times 10^{-2} \text{ min}^{-1}$  for **1** with 1 eq. of mesityl bromide;  $5.6 \times 10^{-2} \text{ min}^{-1}$  for **1** with 10 eq. of mesityl bromide; and  $10.2 \times 10^{-2} \text{ min}^{-1}$  for **1** with 100 eq. of mesityl bromide. However, the RMSR and the fits get progressively worse with increased concentrations of mesityl bromide, and therefore they are unable to accurately account for the subsequent reactivity. The simple three-component models entirely fail to describe the case of **1** with 1000 eq. of mesityl bromide. To improve the models with high concentration of mesityl bromide, we have tried to include more absorbing and non-absorbing species, and we evaluated multiple additional kinetic scenarios. However, since the number of kinetic models grow extensively with the number of species and the interdependence of parameters increase lowering the reliability of the fits, these attempts were also unsuccessful. Particularly, we were unable to correctly fit the decay in the main-absorption feature region at  $\sim 485 \text{ nm}$ . Instead, we compare the extent of conversion of the Ni(II) starting material after 30 minutes of irradiation with varying amounts of mesityl bromide (**Figure S19a**, **Table S2**) by comparing the absorbance decay of **1** at  $485 \text{ nm}$ .

The rate of photochemical decomposition of **2** in neat THF or with a low concentration of mesityl bromide is very small for a reliable exponential fitting model. In the first 30 minutes of irradiation of **2** with 1-100 equivalents of mesityl bromide, the changes in the absorbance are on the order of  $\sim 0.03$  units (**Figure S19b**). Any observed initial rate constants are thus likely associated with higher uncertainty, precluding their direct comparison. Furthermore, as in the case of **1**, we were unable to obtain a reliable kinetic model for the case of **2** with 1000 eq. of mesityl bromide, for which the main-absorption region at  $\sim 507 \text{ nm}$  is fitted incorrectly. Therefore for qualitative purposes, we have also tabulated the percent conversion of **2** after 30 minutes (**Table S2**).

a) Photoirradiation of **1** with varied conc. of mesityl bromide      b) Photoirradiation of **2** with varied conc. of mesityl bromide

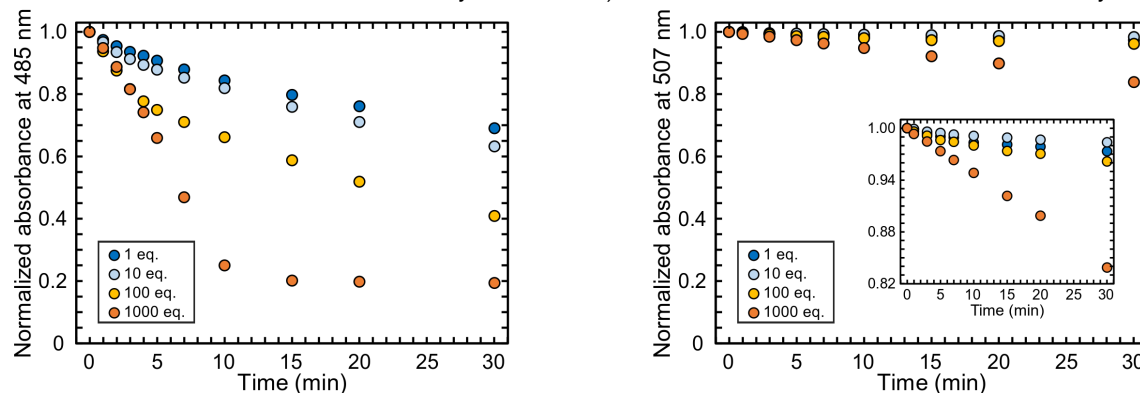


**Figure S19.** Absorbance at the peak maximum of band *i* plotted against time in the first 30 minutes of photoirradiation of **1** and **2** using a 390 nm LED in THF. Irradiations were performed with varied concentrations of mesityl bromide.

**Table S2.** Conversion of **1** and **2** as a function of varied concentration of mesityl bromide after 30 minutes of irradiation with 390 nm LED.

Sample	Conversion (%) after 30 min	Sample	Conversion (%) after 30 min
<b>1</b> + 1 eq. BrMes	30.9	<b>2</b> + 1 eq. BrMes	2.7
<b>1</b> + 10 eq. BrMes	36.7	<b>2</b> + 10 eq. BrMes	1.6
<b>1</b> + 100 eq. BrMes	59.0	<b>2</b> + 100 eq. BrMes	3.8
<b>1</b> + 1000 eq. BrMes	80.5	<b>2</b> + 1000 eq. BrMes	16.1

## S1.6. Transient Absorption Spectroscopy

a) UV-vis stability of **1** over the course of TA      b) UV-vis stability of **1** with 100 eq. mesityl bromide over the course of TA

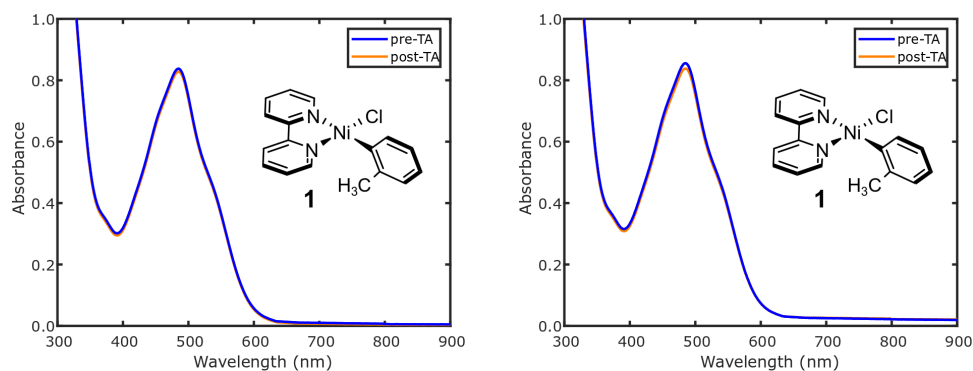


**Figure S20.** UV-vis spectra of complex **1** in THF, collected before and after conducting the TA experiments. a) in the absence of mesityl bromide, b) with 100 eq. mesityl bromide.

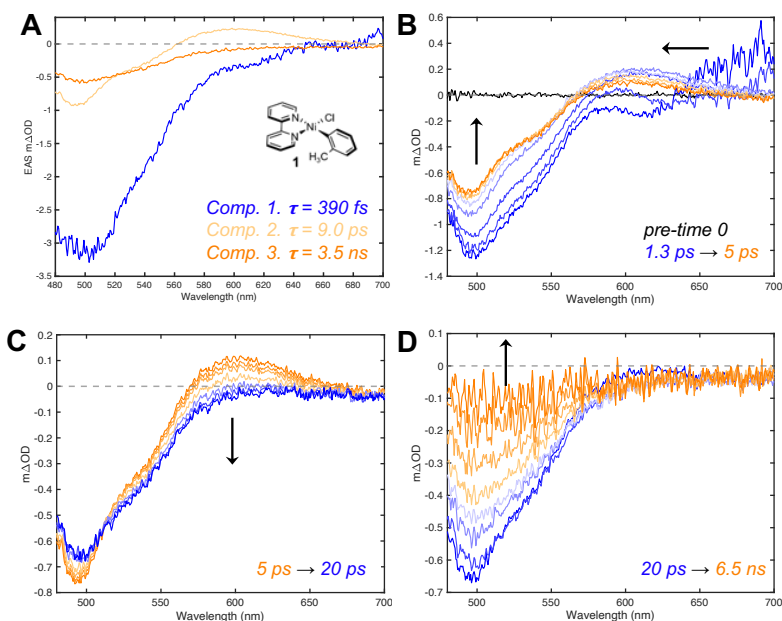


**Figure S21.** Ultrafast TA spectra of **1** in deoxygenated THF upon 400 nm excitation. Evolution-associated spectra obtained from a 3-component, sequential global model of the data (**A**). TA difference spectra for short times (**B**), middle times (**C**), and longer time delays between pump and probe (**D**), with arrows displaying observable trends. Data for each time point was averaged  $\pm 3$  consecutive time points in panel **B**,  $\pm 2$  ps in panel **C**, and  $\pm 10$  ps for times up to 100 ps and  $\pm 100$  ps for 1 ns onward in panel **D** to achieve enhanced signal-to-noise.

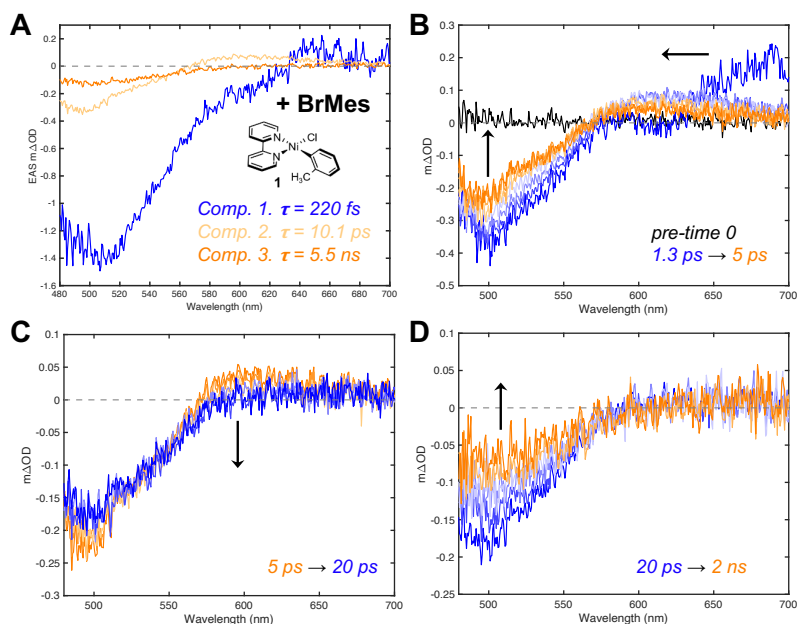


**Figure S22.** Ultrafast TA spectra of **1** + 100 eq. BrMes in deoxygenated THF upon 400 nm excitation. Evolution-associated spectra obtained from a 3-component, sequential global model of the data (**A**). We have fixed the first rate constant such that we could extract a spectral component separate from the cross-phase modulation at ultra-fast times. TA difference spectra for short times (**B**), middle times (**C**), and longer

time delays between pump and probe (**D**), with arrows displaying observable trends. Data for each time point was averaged  $\pm 3$  consecutive time points in panel **B**,  $\pm 2$  ps in panel **C**, and  $\pm 10$  ps for times up to 100s ps and  $\pm 100$  ps for 1 ns onward in panel **D** to achieve enhanced signal-to-noise.

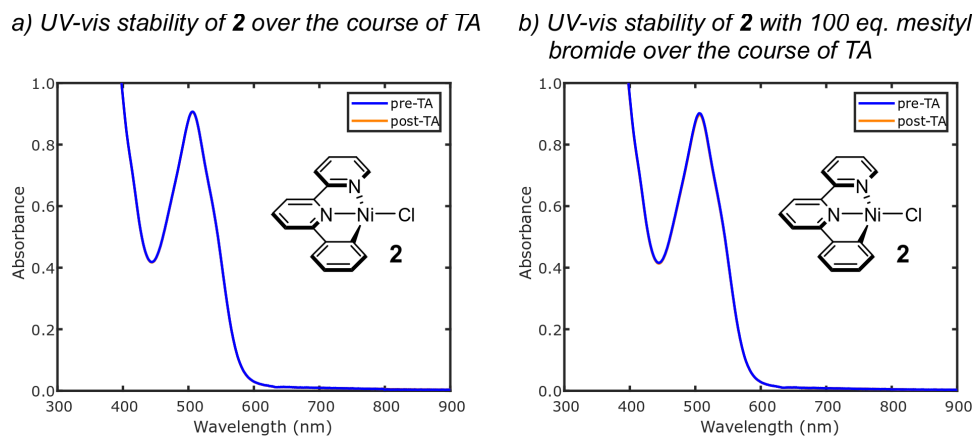


**Figure S23.** UV-vis spectra of complex **2** in THF, collected before and after conducting the TA experiments.

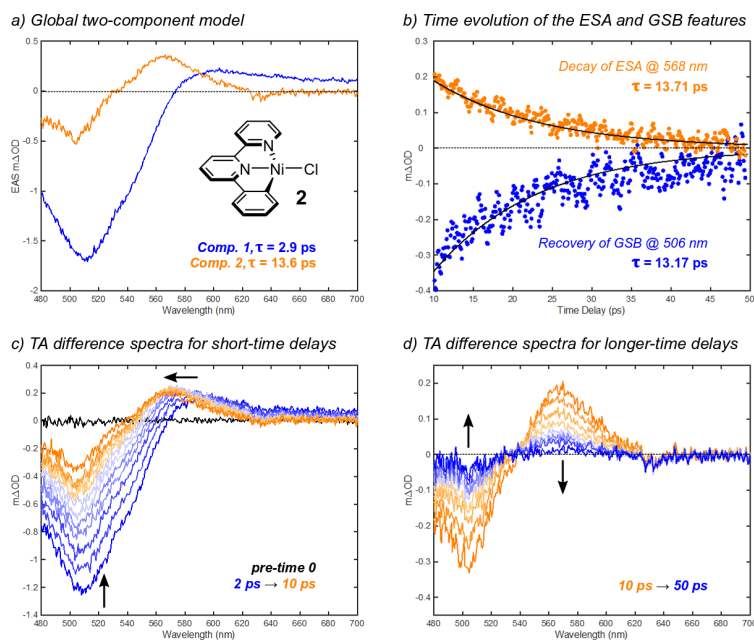


**Figure S24.** Ultrafast TA spectra of **2** in deoxygenated THF upon 400 nm excitation, reproduced from **Figure 6** in the main-text. Evolution-associated spectra obtained from a 2-component, sequential global model of the data (**A**). Decay of the ESA feature at 568 nm ( $13.7 \pm 1.8$  ps, orange) and recovery of the GSB feature at 506 nm ( $13.2 \text{ ps} \pm 1.8 \text{ ps}$ , blue), with their fits to mono-exponential functions in black (**B**). TA difference spectra for short times (**C**) and longer time delays between pump and probe (**D**), with arrows displaying observable trends. Data for each time point was averaged  $\pm 3$  consecutive time points in panel **C** and  $\pm 2$  ps in panel **D** for enhanced signal-to-noise.

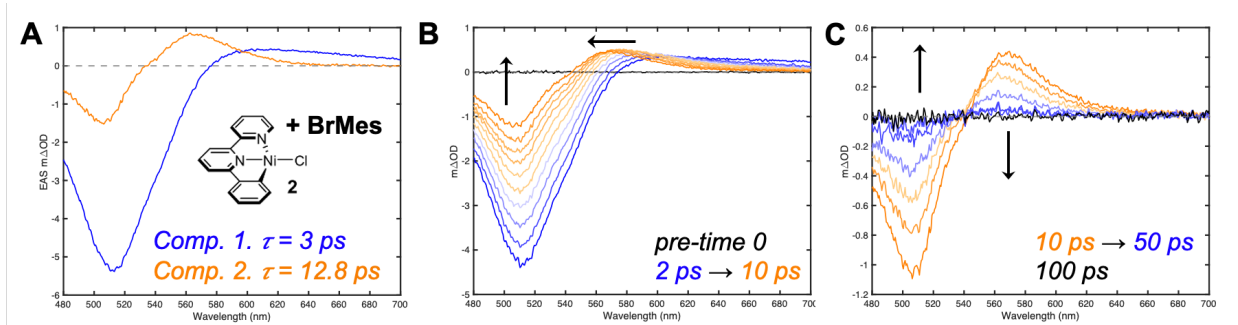


**Figure S25.** Ultrafast TA spectra of **2** + 100 eq. BrMes in deoxygenated THF upon 400 nm excitation. Evolution-associated spectra obtained from a 2-component, sequential global model of the data (A). TA difference spectra for short times (B) and longer time delays between pump and probe (C), with arrows displaying observable trends. Data for each time point was averaged  $\pm 3$  consecutive time points in panel B and  $\pm 2$  ps in panel C for enhanced signal-to-noise.

**Table S3.** Best kinetic parameters obtained by global fitting ultrafast transient absorption data of (un)tethered Ni(II)-bpy aryl halide complexes **1** and **2** in THF to sequential decay models. Error bounds for kinetic rates are determined from a standard error calculation in Glotaran and are reported in parentheses. Comparison with previously-reported relaxation times for complex **1** is included from ref <sup>11</sup>.

Sample	$\lambda_{\text{exc.}}$ (nm)	$k_1$ (ps <sup>-1</sup> )	$k_2$ (ps <sup>-1</sup> )	$k_3$ (ps <sup>-1</sup> )	$\tau_1$ (ps)	$\tau_2$ (ps)	$\tau_3$ (ns)	Pulse Power ( $\mu\text{J/pulse}$ )
<b>1</b>	400	2.550 ( $\pm 0.012$ )	0.112 ( $\pm 0.001$ )	0.00029 ( $\pm 1.10\text{e-}06$ )	0.392	8.96	3.47	0.23
<b>1</b> (ref <sup>11</sup> )	530	–	–	–	0.62 ( $\pm 0.01$ )	5.45 ( $\pm 0.06$ )	4.13 ( $\pm 0.06$ )	0.5
<b>1</b> + 100 eq. BrMes	400	4.5 (fixed)	0.0989 ( $\pm 0.001$ )	0.00018 ( $\pm 2.41\text{e-}06$ )	0.22	10.11	5.50	0.23
<b>2</b>	400	0.345 ( $\pm 0.001$ )	0.0735 ( $\pm 0.00026$ )	–	2.89	13.59	–	0.30
<b>2</b> + 100 eq. BrMes	400	0.331 ( $\pm 0.001$ )	0.0779 ( $\pm 0.00026$ )	–	3.02	12.80	–	0.23



## S2. Computational Section

### S2.1. General Computational Considerations

All the computations were performed using ORCA 5.0 software.<sup>14,15</sup> The molecular structures were optimized with DFT using the BP86 functional<sup>16,17</sup> with def2-TZVPP(Ni)+def2-TZVP basis set,<sup>18</sup> D3BJ dispersion correction,<sup>19,20</sup> and the CPCM solvation model<sup>21,22</sup> (THF). The calculations were expedited by expanding the Coulomb integrals in an auxiliary basis set, the resolution-of-identity (RI-J) approximation.<sup>23</sup> Unrestricted formalism (UKS) was used to optimize lowest-lying singlet and triplet states. Thermal contributions to energy were obtained from frequency calculations performed at the same level of theory with the rigid rotor/harmonic oscillator approximation (for  $p = 1$  bar,  $T = 298$  K). On top of the optimized geometries, the electronic energy terms and molecular properties were evaluated using ab initio complete active space self-consistent field theory with the quasidegenerate N-electron valence state perturbation theory correction (CASSCF/QD-NEVPT2). CASSCF/QD-NEVPT2 methods were used as implemented in ORCA 5.0,<sup>24</sup> in combination with the def2-TZVPP(Ni)+def2-TZVP basis set and CPCM (THF). State-averaged calculations with 15 singlets and 25 triplets were used. Complete active spaces included 10 electrons in 9 orbitals (10e, 9o): Ni 3d(yz), 3d(z<sup>2</sup>), 3d(xy), 3d(xz), a pair of bonding and antibonding Ni 3d(x<sup>2</sup>-y<sup>2</sup>)/aryl C(sp<sup>2</sup>) orbitals, and three bpy  $\pi^*$  orbitals. The active space choice follows our previous study and is showed in **Figure S26**.

Optimized structures of all of the studied complexes are compiled in the **Section S5**.

## S2.2. Electronic Structure Calculations

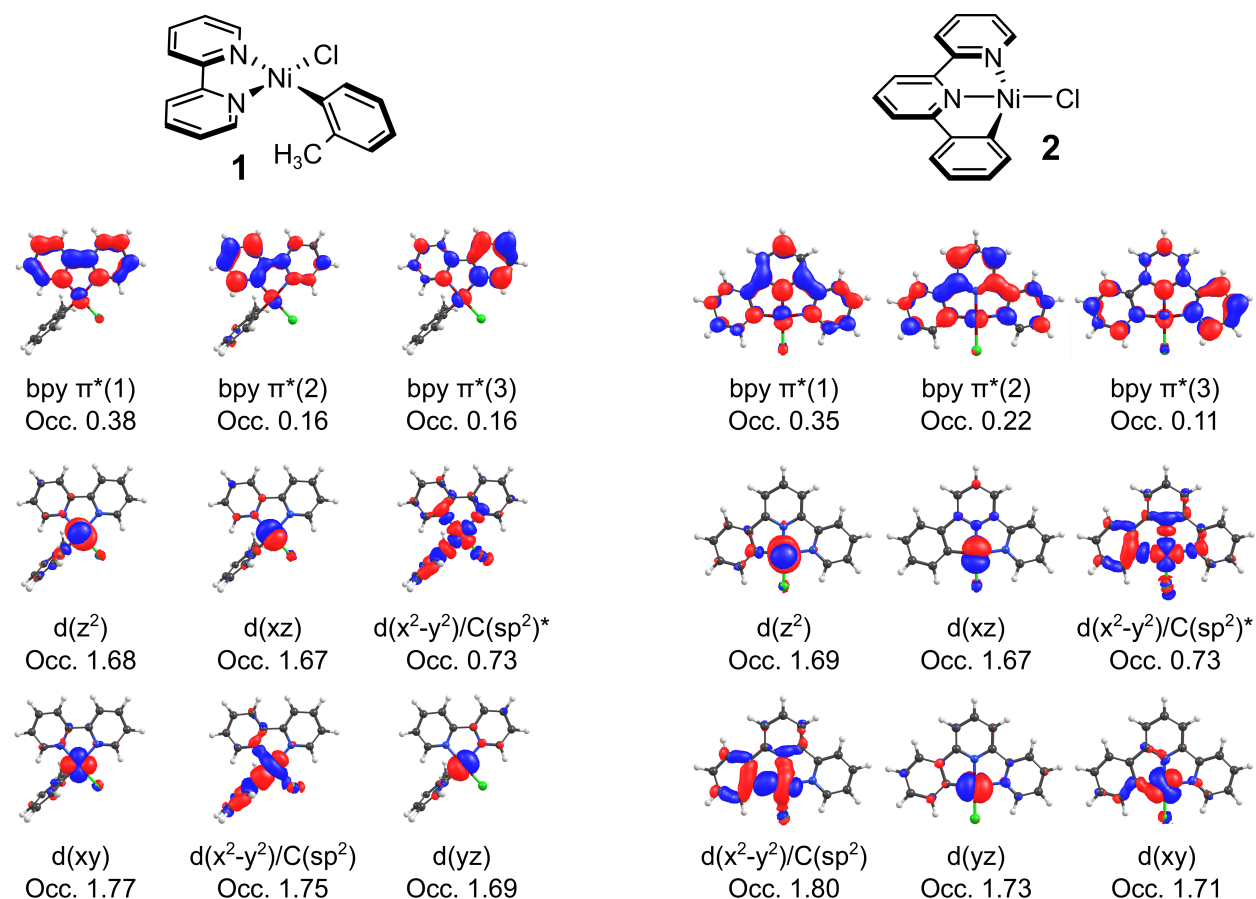


**Figure S26.** Active space given for complexes **1** and **2**, with x-axis oriented along the Ni–halide bond and y-axis along the Ni–aryl bond. The CASSCF complete active space consists of 10 electrons in 9 orbitals (10e, 9o): Ni 3d(yz), 3d( $z^2$ ), 3d(xy), 3d(xz), a pair of bonding and antibonding Ni 3d( $x^2-y^2$ )/aryl C( $sp^2$ ) orbitals, and three bpy  $\pi^*$  orbitals. Occupation numbers are based on Löwdin orbital population analysis.

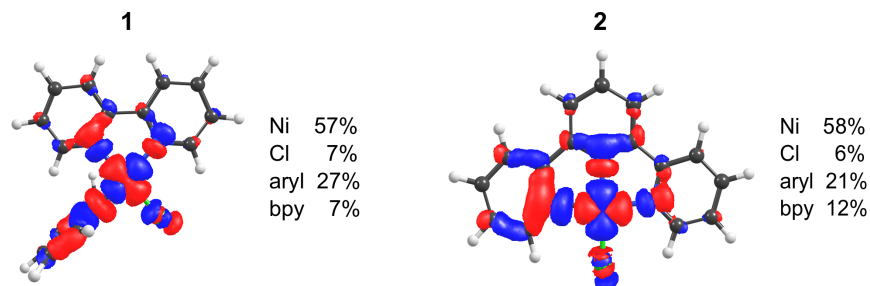


**Figure S27.** Comparison of the unoccupied Ni 3d( $x^2-y^2$ )/C( $sp^2$ )<sup>\*</sup> antibonding acceptor orbitals of **1** and **2**, and sum of the compositions of individual molecular fragments based on Löwdin orbital population analysis.

**Table S4.** CASSCF/NEVPT2 composition of the singlet ground state of complex **1** with CPCM(THF) (10e,9o active space) – 25 triplet roots, 15 singlet roots. Active space orbitals (in order for CI vector notation below): d(xy), d(x<sup>2</sup>-y<sup>2</sup>)/C(sp<sup>2</sup>), d(yz), d(z<sup>2</sup>), d(xz), d(x<sup>2</sup>-y<sup>2</sup>)/C(sp<sup>2</sup>)\*,  $\pi^*(1)$ ,  $\pi^*(2)$ ,  $\pi^*(3)$ .

CI Vector	Transition	Contribution
222220000	Closed-shell singlet (CSS) d <sup>8</sup>	0.573
212221000	d(x <sup>2</sup> -y <sup>2</sup> )/C(sp <sup>2</sup> ) → d(x <sup>2</sup> -y <sup>2</sup> )/C(sp <sup>2</sup> )*	0.124
222210100	d(xz) → $\pi^*(1)$	0.095
222120100	d(z <sup>2</sup> ) → $\pi^*(1)$	0.041
221220001	d(yz) → $\pi^*(3)$	0.028
222210010	d(xz) → $\pi^*(2)$	0.018
221220100	d(yz) → $\pi^*(2)$	0.016
Sum of CSS		57 %
Sum of all MLCTs		20 %
Sum of all LFs		17 %
Sum of mixed MLCTs and LFs		3 %

**Table S5.** CASSCF/NEVPT2 composition of the singlet ground state of complex **2** with CPCM(THF) (10e,9o active space) – 25 triplet roots, 15 singlet roots. Active Space Orbitals (in order for CI vector notation below): d(x<sup>2</sup>-y<sup>2</sup>)/C(sp<sup>2</sup>), d(yz), d(xy), d(z<sup>2</sup>), d(xz), d(x<sup>2</sup>-y<sup>2</sup>)/C(sp<sup>2</sup>)\*,  $\pi^*(1)$ ,  $\pi^*(2)$ ,  $\pi^*(3)$ .

CI Vector	Transition	Contribution
222220000	Closed-shell singlet (CSS) d <sup>8</sup>	0.561
222210100	d(xz) → $\pi^*(1)$	0.168
122221000	d(x <sup>2</sup> -y <sup>2</sup> )/C(sp <sup>2</sup> ) → d(x <sup>2</sup> -y <sup>2</sup> )/C(sp <sup>2</sup> )*	0.116
212220010	d(yz) → $\pi^*(2)$	0.047
022212100	2x[d(x <sup>2</sup> -y <sup>2</sup> )/C(sp <sup>2</sup> )] → 2x[d(x <sup>2</sup> -y <sup>2</sup> )/C(sp <sup>2</sup> )*] + d(xz) → $\pi^*(1)$	0.018
Sum of CSS		56 %
Sum of all MLCTs		22 %
Sum of all LFs		16 %
Sum of mixed MLCTs and LFs		4 %

**Table S6.** Complex **1**: CASSCF/QD-NEVPT2 spin-orbit corrected absorption transitions for the CPCM(THF) phase spectrum (10e,9o Active Space) – 25 triplet roots, 15 singlet roots.

#	Energy (cm <sup>-1</sup> )	Wavelength (nm)	$f_{osc}$	Main Character
1	13402	746	0.00293	<sup>3</sup> MLCT
2	14907	671	0.01738	<sup>3</sup> MLCT
3	14918	670	0.00552	<sup>3</sup> MLCT
4	15422	648	0.00483	<sup>3</sup> LF
5	15999	625	0.02866	<sup>1</sup> MLCT
6	17179	582	0.27217	<sup>1</sup> MLCT
7	17290	578	0.04568	<sup>3</sup> MLCT
8	21987	455	0.03244	<sup>1</sup> LF
9	22366	447	0.02119	<sup>1</sup> MLCT

10	22618	442	0.00139	<sup>3</sup> MLCT
11	22641	442	0.00122	<sup>3</sup> MLCT
12	23167	432	0.00637	<sup>1</sup> LF
13	23565	424	0.05144	<sup>1</sup> LF
14	23840	420	0.00225	<sup>3</sup> MLCT
15	23883	419	0.00135	<sup>3</sup> MLCT
16	25469	393	0.00360	<sup>3</sup> MLCT
17	25513	392	0.00468	<sup>3</sup> MLCT
18	25546	391	0.00438	<sup>1</sup> MLCT
19	27192	368	0.03055	<sup>3</sup> MLCT
20	27648	362	0.14485	<sup>1</sup> MLCT
21	29515	339	0.01377	<sup>3</sup> MLCT
22	30215	331	0.21383	<sup>1</sup> MLCT

**Table S7.** Complex **2**: CASSCF/QD-NEVPT2 spin-orbit corrected absorption transitions for the CPCM(THF) phase spectrum (10e,9o Active Space) – 25 triplet roots, 15 singlet roots.

#	Energy (cm <sup>-1</sup> )	Wavelength (nm)	$f_{osc}$	Main Character
1	14837	674	0.00167	<sup>3</sup> MLCT
2	15128	661	0.00113	<sup>1</sup> MLCT
3	16011	625	0.00245	<sup>3</sup> MLCT
4	16389	610	0.00400	<sup>3</sup> MLCT
5	17341	577	0.05300	<sup>1</sup> MLCT
6	17756	563	0.00661	<sup>3</sup> MLCT
7	18618	537	0.08487	<sup>1</sup> MLCT
8	21332	469	0.01242	<sup>1</sup> MLCT
9	21598	463	0.01840	<sup>1</sup> MLCT
10	22728	440	0.00666	<sup>3</sup> MLCT
11	22781	439	0.00219	<sup>3</sup> MLCT
12	23395	427	0.09178	<sup>1</sup> LF
13	24333	411	0.00236	<sup>3</sup> MLCT
14	25695	389	0.02100	<sup>1</sup> LF
15	27170	368	0.07812	<sup>1</sup> LF
16	30430	329	0.00326	<sup>3</sup> MLCT
17	30626	327	0.00237	<sup>1</sup> MLCT
18	32347	309	0.00594	<sup>3</sup> MLCT
19	32440	308	0.04757	<sup>1</sup> MLCT

**Table S8.** Homolytic Ni(II)–C(sp<sup>2</sup>) vs. Ni(II)–Cl bond-dissociation energies (BDEs) of **1** and **2** at the DFT (B3LYP) level.

Complex	Ni(II)–C(sp <sup>2</sup> ) BDE (kcal mol <sup>-1</sup> )	Ni(II)–Cl BDE (kcal mol <sup>-1</sup> )
<b>1</b>	48.4	89.7
<b>2</b>	50.2	98.0

Note that energies presented in **Table S8** are obtained from B3LYP single-point calculations on top of the BP86-D3BJ(CPCM, THF) optimized structures as described in Computational Details **Section S2.1** using the same def2-TZVPP(Ni)+def2-TZVP basis set. Each value of BDE is derived from two separate calculations of Ni(I) and aryl or chlorine radical; for tethered **2**, the Ni(II)–C(sp<sup>2</sup>) BDE is obtained from single calculation of the optimized structure of **2** with dissociated aryl ligand, but tethered to the bipyridine unit.

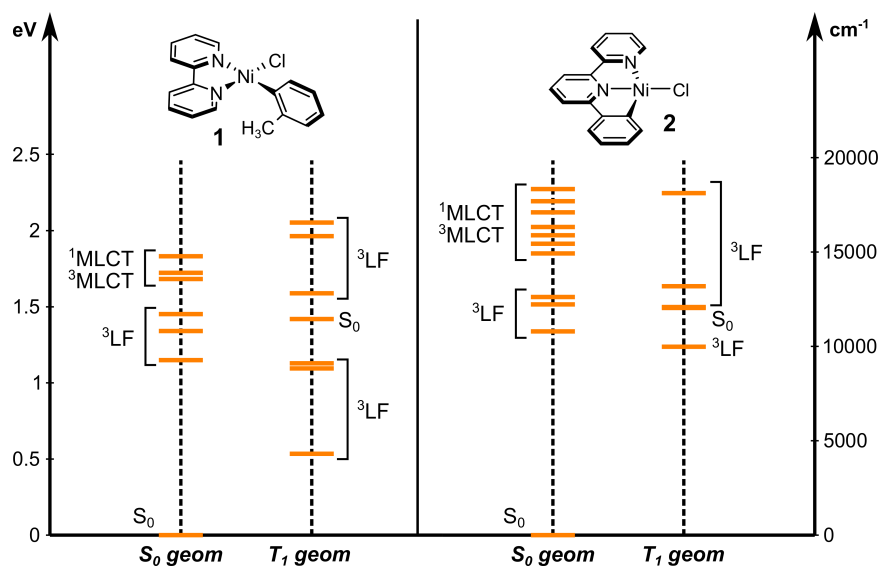


**Figure S28.** Electronic energy diagrams of singlet and triplet geometries of complexes **1** and **2** calculated with CASSCF/QD-NEVPT2 method with 10e,9o active space. The excitations are characterized as MLCT or LF transitions based on the configuration with the largest weight in the specific excited-state CI vector.

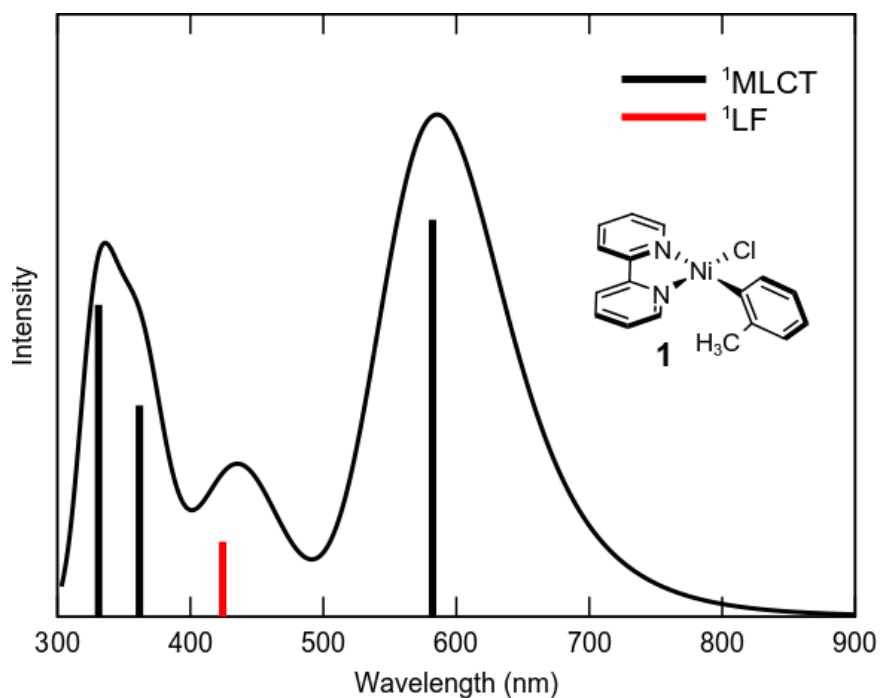


**Figure S29.** Calculated UV-vis spectra of complex **1** at the spin-orbit corrected CASSCF/QD-NEVPT2 level with 10e,9o active space. The most intense excitations are highlighted and characterized as  $^1\text{MLCT}$  or  $^1\text{LF}$  transitions.

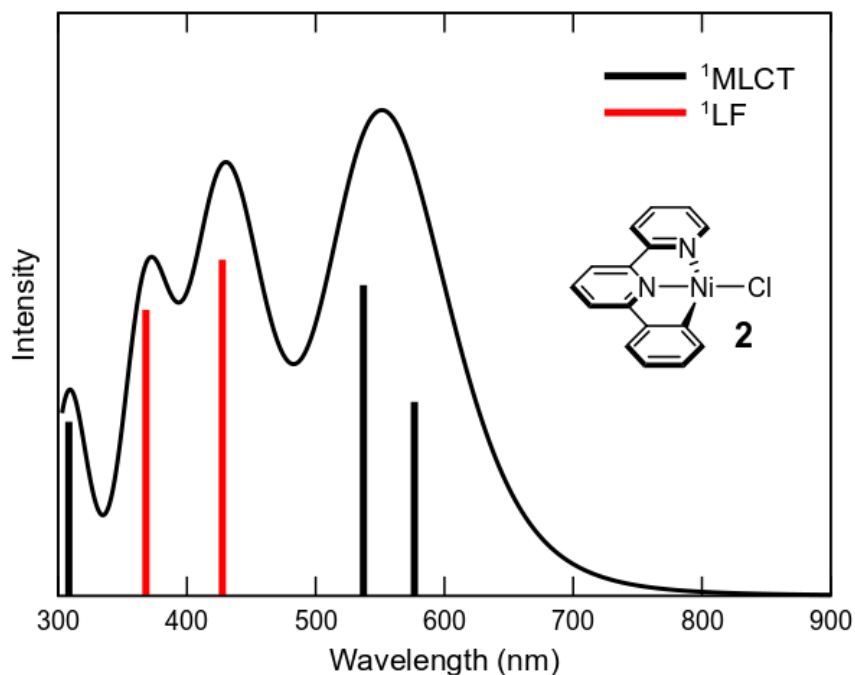


**Figure S30.** Calculated UV-vis spectra of complex **2** at the spin-orbit corrected CASSCF/QD-NEVPT2 level with 10e,9o active space. The most intense excitations are highlighted and characterized as  $^1\text{MLCT}$  or  $^1\text{LF}$  transitions.

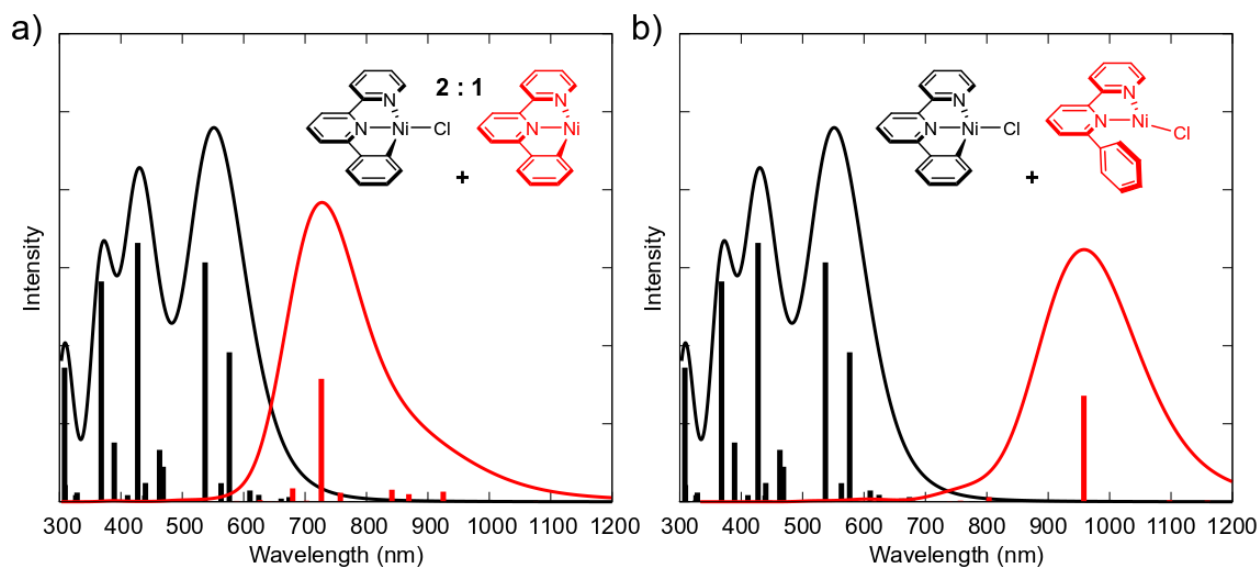


**Figure S31.** Calculated UV-vis spectra of complex **2** with a) tethered, tridentate Ni(I)-bpy phenyl intermediate and b) tridentate Ni(I)- $\text{Phbpy}$  chloride intermediate, using the spin-orbit corrected CASSCF/QD-NEVPT2 level. The calculated oscillator strengths of Ni(I)-bpy phenyl have been scaled to maintain 2:1 ratio of parent Ni(II) complex and tridentate Ni(I) intermediate.

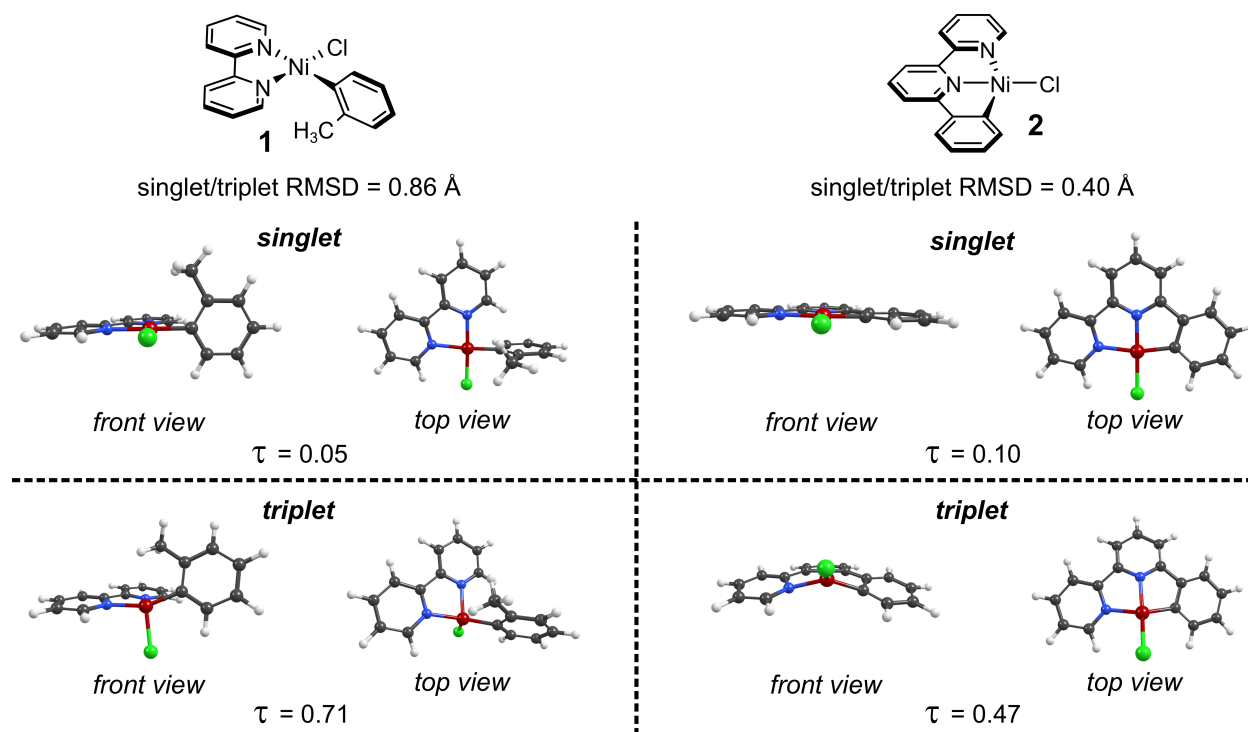


**Figure S32.** To evaluate the amount of stabilization of the lowest-lying triplet excited state through geometry distortion, we have optimized the geometries of complexes **1** and **2** in the singlet and triplet electronic states and computed the  $\tau$  angles;  $\tau = (360^\circ - (\alpha + \beta))/(141^\circ)$ , where  $\alpha$  and  $\beta$  are the two largest angles between the Ni coordinating atoms. The parameter  $\tau$  was defined as a four-coordinate geometry index ranging from perfect tetrahedral ( $\tau = 1$ ) to perfect square planar ( $\tau = 0$ ) geometry.<sup>25</sup> In the case of complex **1** in the singlet and triplet states, the  $\tau = 0.05$  (singlet) and  $\tau = 0.71$  (triplet) were obtained. This indicates a perfect square-planar geometry in the singlet state and a pseudo-tetrahedral geometry in the triplet state. For complex **2**, the  $\tau$  values significantly deviate from the perfect structures, particularly for the triplet-state geometry;  $\tau = 0.10$  (singlet) and  $\tau = 0.47$  (triplet). RMSD = root-mean-square deviation of atomic positions between superimposed structures of optimized singlet and triplet states.



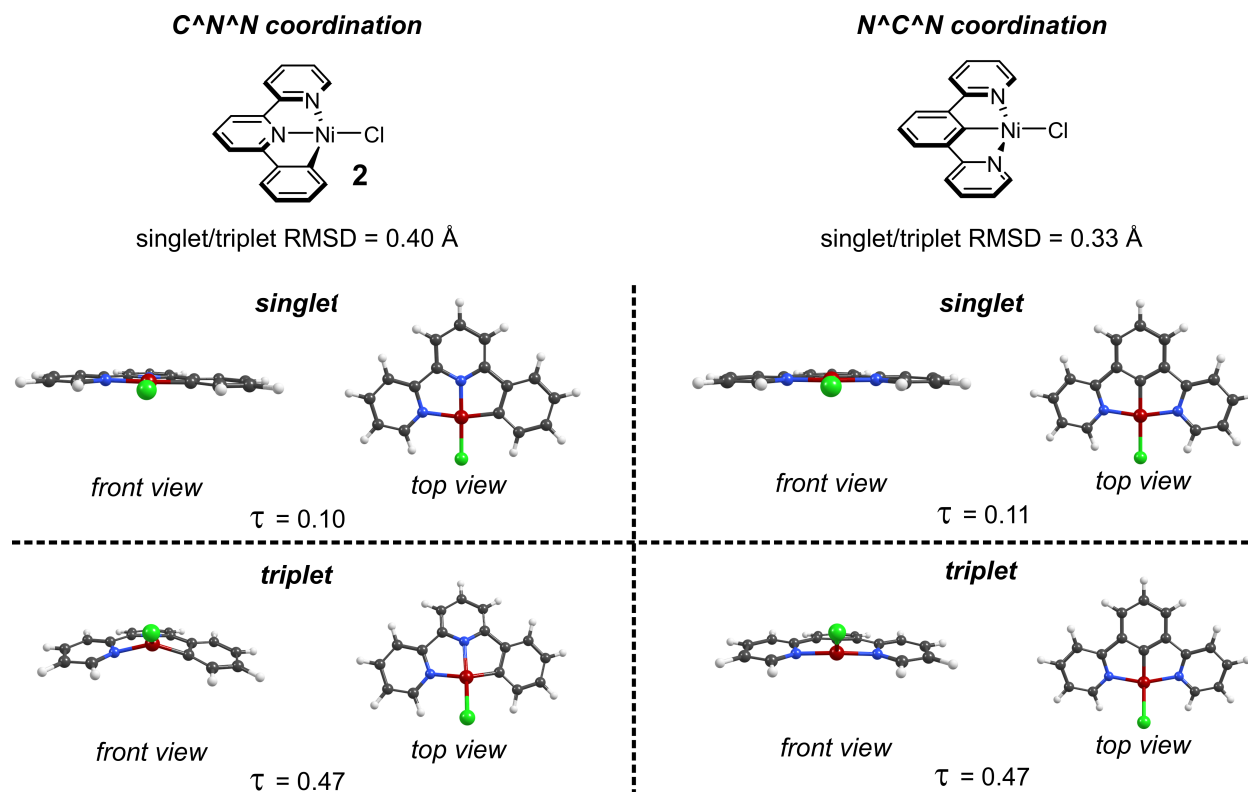


**Figure S33.** Comparison of the optimized singlet and triplet geometries of tethered **2** with C<sup>^</sup>N<sup>^</sup>N coordination vs. analogous complex with N<sup>^</sup>C<sup>^</sup>N coordination.  $\tau = (360^\circ - (\alpha + \beta))/(141^\circ)$ , where  $\alpha$  and  $\beta$  are the two largest angles between the Ni coordinating atoms. RMSD = root-mean-square deviation of atomic positions between superimposed structures of optimized singlet and triplet states.

## S3. References

- (1) Cagan, D. A.; Bím, D.; Silva, B.; Kazmierczak, N. P.; McNicholas, B. J.; Hadt, R. G. Elucidating the Mechanism of Excited-State Bond Homolysis in Nickel–Bipyridine Photoredox Catalysts. *J. Am. Chem. Soc.* **2022**, *144* (14), 6516–6531. <https://doi.org/10.1021/jacs.2c01356>.
- (2) Vogt, N.; Sandleben, A.; Kletsch, L.; Schäfer, S.; Chin, M. T.; Vicic, D. A.; Hörner, G.; Klein, A. Role of the X Coligands in Cyclometalated [Ni(Phbpy)X] Complexes (HPhbpy = 6-Phenyl-2,2'-Bipyridine). *Organometallics* **2021**, *40* (11), 1776–1785. <https://doi.org/10.1021/acs.organomet.1c00237>.
- (3) Mullen, K. M.; van Stokkum, I. H. M. TIMP: An R Package for Modeling Multi-Way Spectroscopic Measurements. *J. Stat. Softw.* **2007**, *18* (3), 1–46. <https://doi.org/10.18637/jss.v018.i03>.
- (4) Snellenburg, J. J.; Laptinok, S.; Seger, R.; Mullen, K. M.; van Stokkum, I. H. M. Glotaran: A Java-Based Graphical User Interface for the R Package TIMP. *J. Stat. Softw.* **2012**, *49* (3), 1–22. <https://doi.org/10.18637/jss.v049.i03>.
- (5) Klein, A.; Rausch, B.; Kaiser, A.; Vogt, N.; Krest, A. The Cyclometalated Nickel Complex [(Phbpy)NiBr] (Phbpy = 2,2'-Bipyridine-6-Phen-2-Yl) – Synthesis, Spectroscopic and Electrochemical Studies. *J. Organomet. Chem.* **2014**, *774*, 86–93. <https://doi.org/https://doi.org/10.1016/j.jorganchem.2014.10.013>.
- (6) Xu, P.-P.; Liao, J.-Y.; Zhang, J.-J.; Shi, W.-M.; Liang, C.; Su, G.-F.; Mo, D.-L. Nickel(II)-Catalyzed [3 + 2] Cycloaddition of Nitrones and Allenates to Access N-Vinylindoles and N-Vinylpyrroles. *Org. Lett.* **2021**, *23* (19), 7482–7486. <https://doi.org/10.1021/acs.orglett.1c02695>.
- (7) Cagan, D. A.; Bím, D.; McNicholas, B. J.; Kazmierczak, N. P.; Oyala, P. H.; Hadt, R. G. Photogenerated Ni(I)–Bipyridine Halide Complexes: Structure–Function Relationships for Competitive C(Sp<sup>2</sup>)–Cl Oxidative Addition and Dimerization Reactivity Pathways. *Inorg. Chem.* **2023**, *62* (24), 9538–9551. <https://doi.org/10.1021/acs.inorgchem.3c00917>.
- (8) Yang, L.; Lu, H.-H.; Lai, C.-H.; Li, G.; Zhang, W.; Cao, R.; Liu, F.; Wang, C.; Xiao, J.; Xue, D. Light-Promoted Nickel Catalysis: Etherification of Aryl Electrophiles with Alcohols Catalyzed by a Ni(II)-Aryl Complex. *Angew. Chemie Int. Ed.* **2020**, *59* (31), 12714–12719. <https://doi.org/https://doi.org/10.1002/anie.202003359>.
- (9) Klein, A.; Kaiser, A.; Wielandt, W.; Belaj, F.; Wendel, E.; Bertagnolli, H.; Zális, S. Halide Ligands—More Than Just  $\sigma$ -Donors? A Structural and Spectroscopic Study of Homologous Organonickel Complexes. *Inorg. Chem.* **2008**, *47* (23), 11324–11333. <https://doi.org/10.1021/ic8007365>.
- (10) Feth, M. P.; Klein, A.; Bertagnolli, H. Investigation of the Ligand Exchange Behavior of Square-Planar Nickel(II) Complexes by X-Ray Absorption Spectroscopy and X-Ray Diffraction. *Eur. J. Inorg. Chem.* **2003**, *2003* (5), 839–852. <https://doi.org/https://doi.org/10.1002/ejic.200390114>.
- (11) Ting, S. I.; Garakyaraghi, S.; Taliaferro, C. M.; Shields, B. J.; Scholes, G. D.; Castellano, F. N.; Doyle, A. G. 3d-d Excited States of Ni(II) Complexes Relevant to Photoredox Catalysis: Spectroscopic Identification and Mechanistic Implications. *J. Am. Chem. Soc.* **2020**, *142* (12), 5800–5810. <https://doi.org/10.1021/jacs.0c00781>.
- (12) Ting, S. I.; Williams, W. L.; Doyle, A. G. Oxidative Addition of Aryl Halides to a Ni(I)-Bipyridine Complex. *J. Am. Chem. Soc.* **2022**, *144* (12), 5575–5582. <https://doi.org/10.1021/jacs.2c00462>.
- (13) Till, N. A.; Oh, S.; MacMillan, D. W. C.; Bird, M. J. The Application of Pulse Radiolysis to the Study of Ni(I) Intermediates in Ni-Catalyzed Cross-Coupling Reactions. *J. Am. Chem. Soc.* **2021**, *143* (25), 9332–9337. <https://doi.org/10.1021/jacs.1c04652>.
- (14) Neese, F. The ORCA Program System. *WIREs Comput. Mol. Sci.* **2012**, *2* (1), 73–78. <https://doi.org/https://doi.org/10.1002/wcms.81>.
- (15) Neese, F. Software Update: The ORCA Program System, Version 4.0. *WIREs Comput. Mol. Sci.* **2018**, *8* (1), e1327. <https://doi.org/https://doi.org/10.1002/wcms.1327>.
- (16) Perdew, J. P. Density-Functional Approximation for the Correlation Energy of the Inhomogeneous

- Electron Gas. *Phys. Rev. B* **1986**, 33 (12), 8822–8824. <https://doi.org/10.1103/PhysRevB.33.8822>.
- (17) Becke, A. D. Density-Functional Exchange-Energy Approximation with Correct Asymptotic Behavior. *Phys. Rev. A* **1988**, 38 (6), 3098–3100. <https://doi.org/10.1103/PhysRevA.38.3098>.
  - (18) Weigend, F.; Ahlrichs, R. Balanced Basis Sets of Split Valence, Triple Zeta Valence and Quadruple Zeta Valence Quality for H to Rn: Design and Assessment of Accuracy. *Phys. Chem. Chem. Phys.* **2005**, 7 (18), 3297–3305. <https://doi.org/10.1039/b508541a>.
  - (19) Grimme, S.; Antony, J.; Ehrlich, S.; Krieg, H. A Consistent and Accurate Ab Initio Parametrization of Density Functional Dispersion Correction (DFT-D) for the 94 Elements H-Pu. *J. Chem. Phys.* **2010**, 132 (15). <https://doi.org/10.1063/1.3382344>.
  - (20) Grimme, S.; Ehrlich, S.; Goerigk, L. Effect of the Damping Function in Dispersion Corrected Density Functional Theory. *J. Comput. Chem.* **2011**, 32 (7), 1456–1465. <https://doi.org/https://doi.org/10.1002/jcc.21759>.
  - (21) Barone, V.; Cossi, M. Quantum Calculation of Molecular Energies and Energy Gradients in Solution by a Conductor Solvent Model. *J. Phys. Chem. A* **1998**, 102 (11), 1995–2001. <https://doi.org/10.1021/jp9716997>.
  - (22) Klamt, A.; Schüürmann, G. COSMO: A New Approach to Dielectric Screening in Solvents with Explicit Expressions for the Screening Energy and Its Gradient. *J. Chem. Soc. Perkin Trans. 2* **1993**, No. 5, 799–805. <https://doi.org/10.1039/P29930000799>.
  - (23) Eichkorn, K.; Treutler, O.; Öhm, H.; Häser, M.; Ahlrichs, R. Auxiliary Basis Sets to Approximate Coulomb Potentials. *Chem. Phys. Lett.* **1995**, 240 (4), 283–290. [https://doi.org/10.1016/0009-2614\(95\)00621-A](https://doi.org/10.1016/0009-2614(95)00621-A).
  - (24) Lang, L.; Sivalingam, K.; Neese, F. The Combination of Multipartitioning of the Hamiltonian with Canonical Van Vleck Perturbation Theory Leads to a Hermitian Variant of Quasidegenerate N-Electron Valence Perturbation Theory. *J. Chem. Phys.* **2020**, 152 (1), 14109. <https://doi.org/10.1063/1.5133746>.
  - (25) Yang, L.; Powell, D. R.; Houser, R. P. Structural Variation in Copper(i) Complexes with Pyridylmethanamide Ligands: Structural Analysis with a New Four-Coordinate Geometry Index, T4. *Dalt. Trans.* **2007**, No. 9, 955–964. <https://doi.org/10.1039/B617136B>.

## S4. NMR Spectra

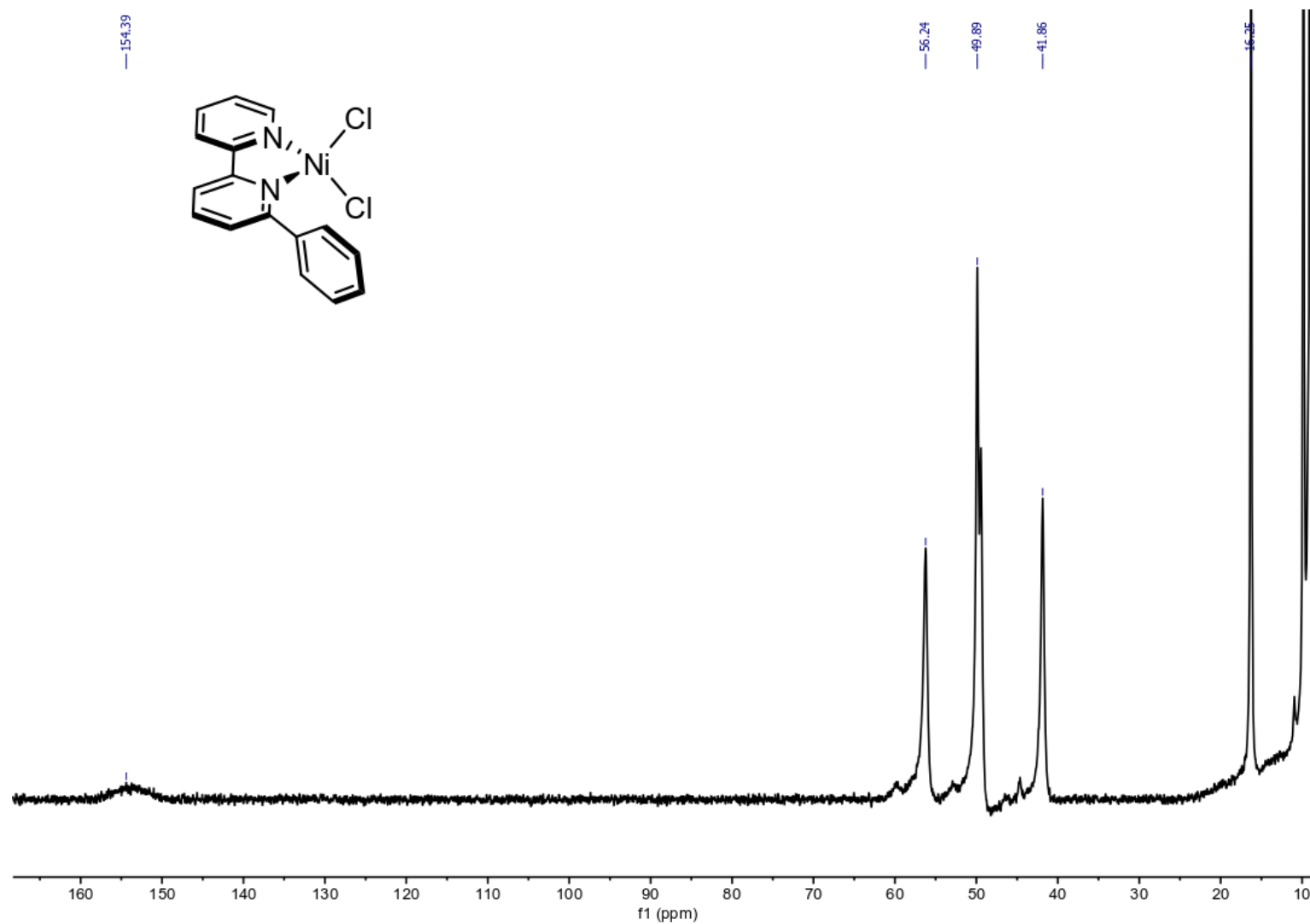


**Figure S34.**  $^1\text{H}$ -NMR (400 MHz,  $\text{CD}_2\text{Cl}_2$ ) spectrum of  $\text{Ni}(\text{PhBpy})\text{Cl}_2$  (paramagnetic region).

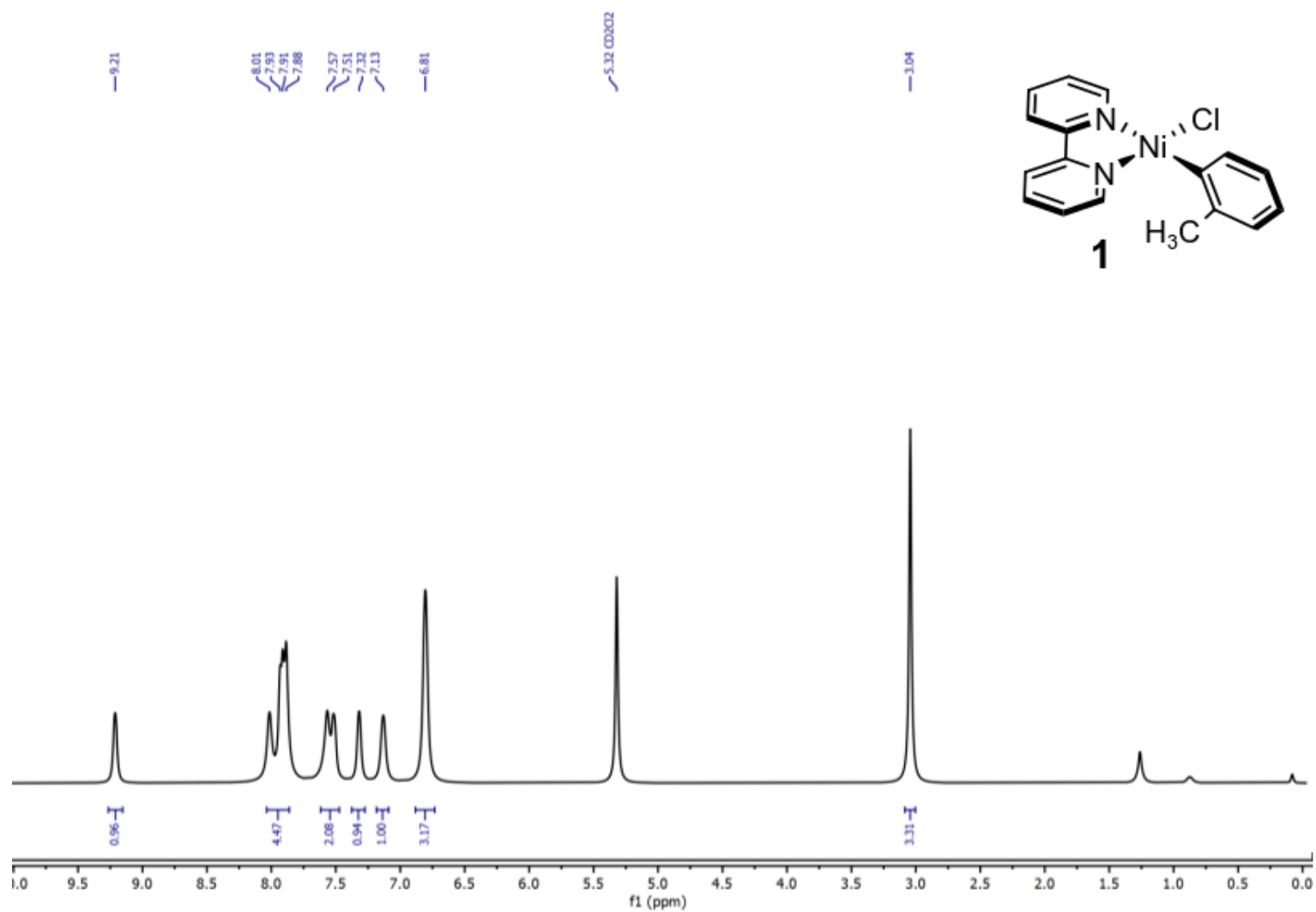


**Figure S35.** <sup>1</sup>H-NMR (400 MHz, CD<sub>2</sub>Cl<sub>2</sub>) spectrum of complex **1**.

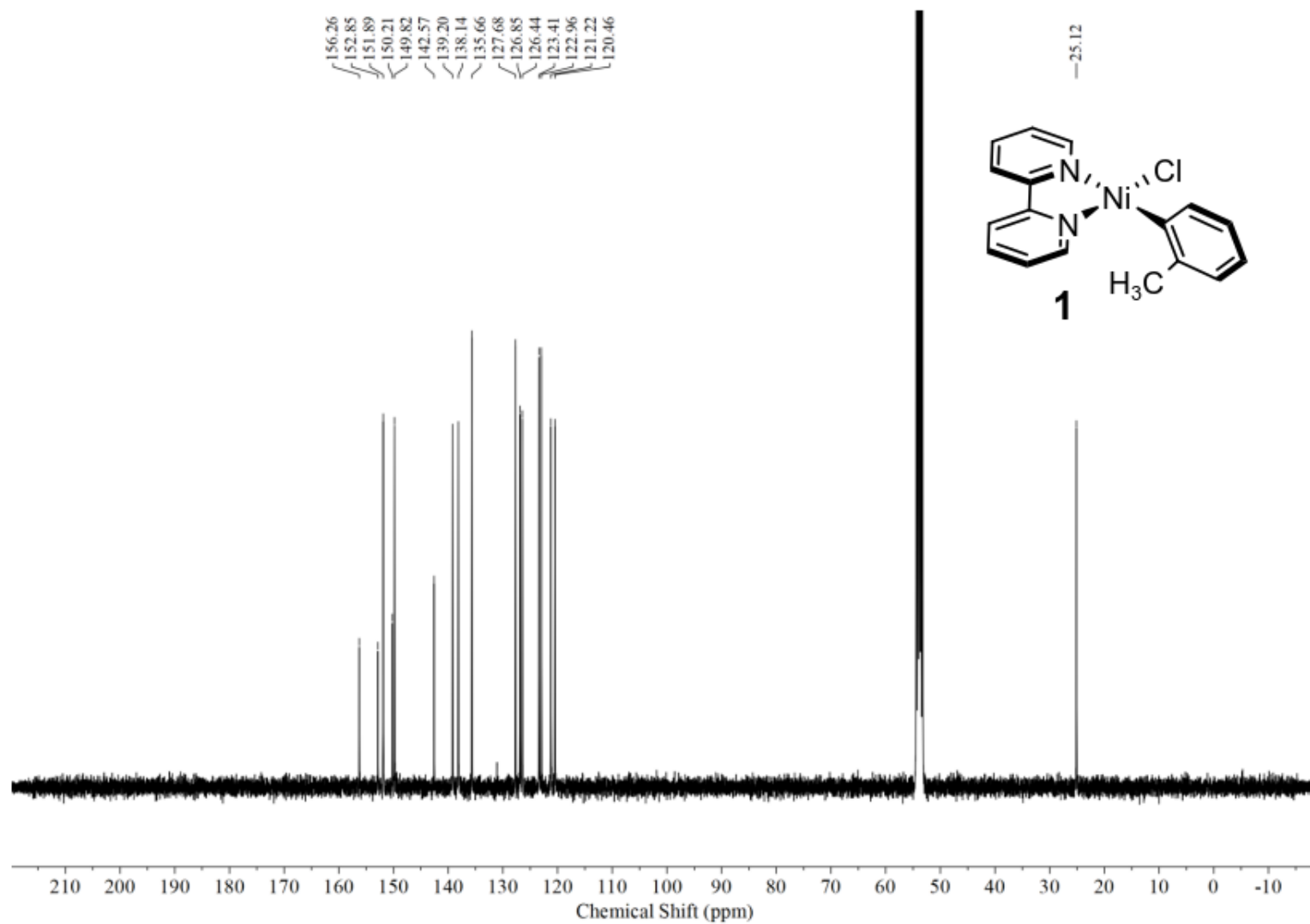


**Figure S36.**  $^{13}\text{C}\{^1\text{H}\}$ -NMR (400 MHz,  $\text{CD}_2\text{Cl}_2$ ) spectrum of complex **1**.

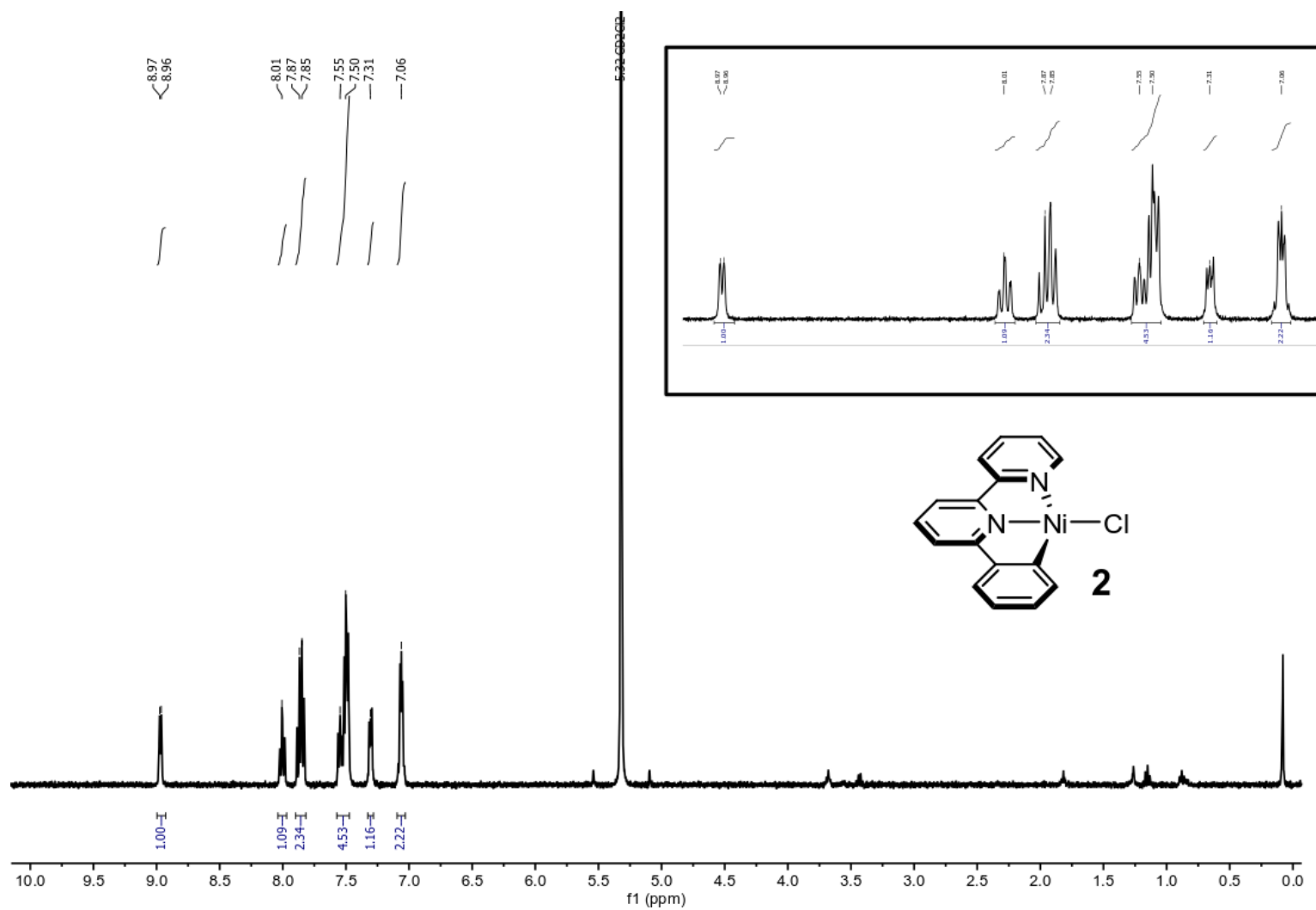


**Figure S37.**  $^1\text{H}$ -NMR (400 MHz,  $\text{CD}_2\text{Cl}_2$ ) spectrum of complex **2**.

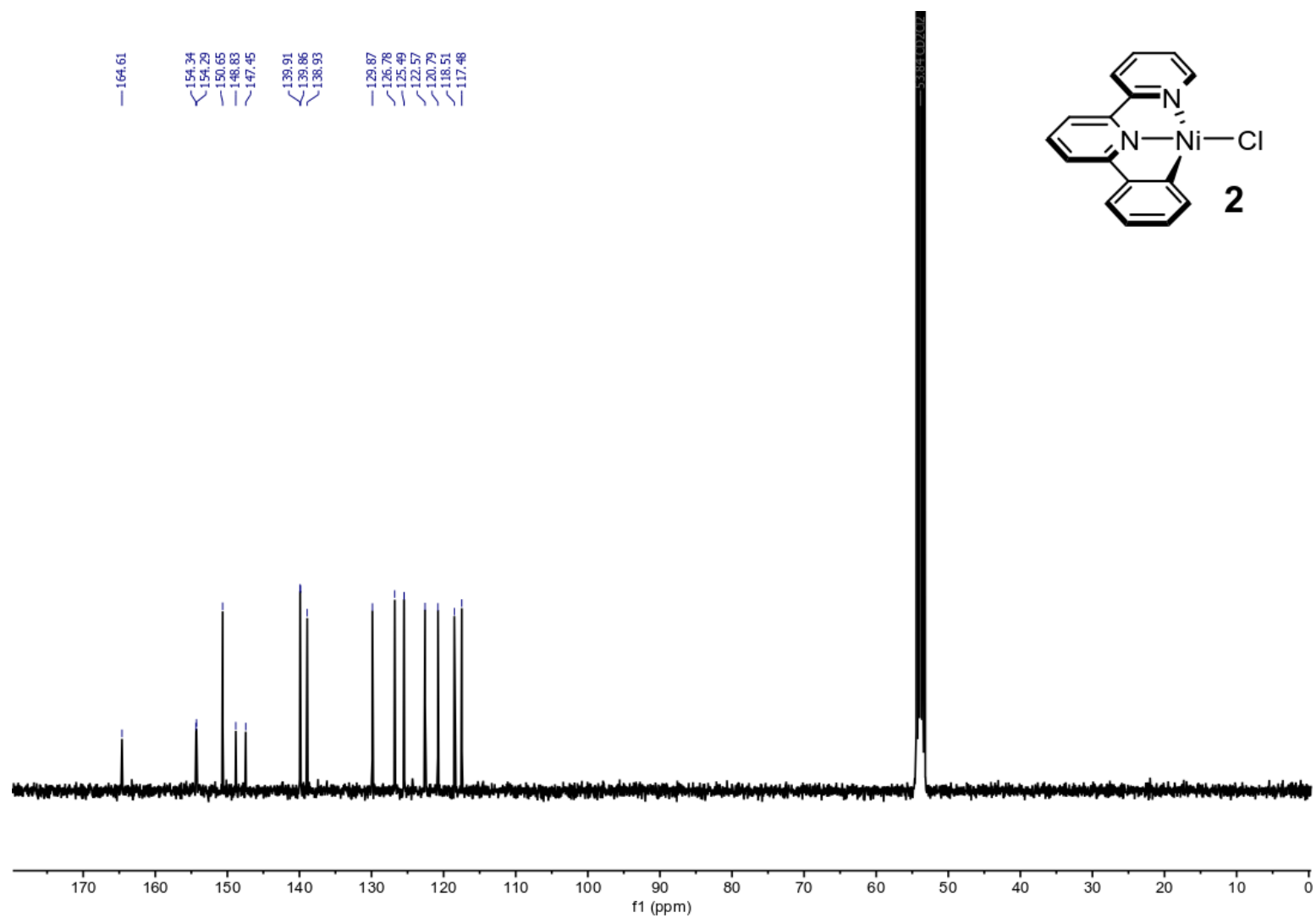


**Figure S38.**  $^{13}\text{C}\{^1\text{H}\}$ -NMR (400 MHz,  $\text{CD}_2\text{Cl}_2$ ) spectrum of complex 2.



## S5. XYZ Structures

36

Complex 1, singlet

C	-4.61552474959046	-0.40820491978595	-0.02635024897933
C	-3.72863856661945	-1.47823970839156	-0.12229237633348
C	-4.10737462151984	0.87965563948017	0.16036427429044
C	-2.72807894945612	1.05203647388707	0.24558181139814
N	-1.86923288679892	0.02294470011971	0.15346991323625
C	-2.35491546049507	-1.23370366301741	-0.02982819172820
C	-1.31783734122486	-2.26630203462947	-0.11476014348968
N	-0.03059283375461	-1.80345249883862	0.00904190286539
C	-1.59181510496072	-3.62208661996073	-0.30672212012205
H	-4.10068605978958	-2.49068227448401	-0.26744067826224
H	-5.69003695228809	-0.57909015566802	-0.09631621523286
H	-4.76525638827404	1.74391937191299	0.24109885169289
H	-2.26769348127167	2.03026116131476	0.39247202196157
C	-0.54621462215391	-4.53782718959666	-0.37748531025210
H	-2.62365014837879	-3.95466674839762	-0.40185760058784
C	0.76083429072327	-4.06483227668604	-0.24861699315621
H	-0.74893797943295	-5.59764439970670	-0.53012073480382
C	0.97619672750969	-2.70539351223914	-0.05698498691241
H	1.61765094190659	-4.73551345318947	-0.29496494038394
H	1.98004705809560	-2.30169034744210	0.04981950954527
Ni	0.16234107641474	0.09889849071909	0.24904737767362
C	2.05614649374364	0.02530819031639	0.32342145921998
C	2.81987742328163	0.04040534545161	-0.86358693651356
C	2.69781525198323	-0.12110193019746	1.56117132874437
C	4.08765439274844	-0.28849961241472	1.63476320203166
C	4.84713410809256	-0.29489637651518	0.46268476503540
C	4.21249937067158	-0.12363619615000	-0.77180026289198
C	2.16081080030590	0.20799695695103	-2.20967886848379
H	4.80479637759795	-0.11790695941085	-1.69112304882718
H	5.93020649022922	-0.42503762439778	0.50692029497482
H	2.11305620978332	-0.11475517001698	2.48412311361511
H	4.57000427527191	-0.41257428601997	2.60672600803576
Cl	0.29814965924915	2.25547791884270	0.50930425751090
H	2.90477361625169	0.24939664727056	-3.01746331878626
H	1.55933202607025	1.12911005799778	-2.23766251611451
H	1.47079855607869	-0.62472799710739	-2.42047359997013

## Complex 1, triplet

C	-4.47593605688499	-0.09491196950643	-0.54230541390839
C	-3.68479423028924	-1.24191539243776	-0.55495161525160
C	-3.91530563173187	1.11599609774983	-0.12796293797883
C	-2.57631932516240	1.13555278712805	0.25330377945890
N	-1.80677530053684	0.03414315094008	0.23326616302934
C	-2.34685969626539	-1.15037315189754	-0.15813110573109
C	-1.41856063136135	-2.29372312809282	-0.10658057292895
N	-0.19017922859439	-2.00490032984501	0.39805652243879
C	-1.73067640291968	-3.59010928816028	-0.52917136263122
H	-4.10673872855441	-2.19752066441472	-0.86141436459373
H	-5.52126385253871	-0.14739284800556	-0.84701029724187
H	-4.50192370450883	2.03328181910972	-0.09816537331012
H	-2.09045420928471	2.05288607911532	0.58822875591100
C	-0.77286236182304	-4.59443036253363	-0.40678231581774
H	-2.70974730582370	-3.81147801051095	-0.95078014575400
C	0.47857139749337	-4.28452157010058	0.13256537811302
H	-1.00143620462408	-5.60993574931588	-0.73038162590686
C	0.73446860810635	-2.97185566806693	0.51705610607196
H	1.25090762166831	-5.04331034760424	0.25109839466383
H	1.69678445996852	-2.66061281073778	0.92342499835303
Ni	0.15959912188675	-0.08332345110650	0.73244938912903
C	2.06864801622060	0.09641201248010	0.41509338654978
C	2.51001249176038	-0.05639230842473	-0.92330358140929
C	3.03285703813010	0.31631688283681	1.41204189740980
C	4.39908075989608	0.39478646270080	1.11119152750673
C	4.82455082454725	0.24972071910821	-0.21235130946946
C	3.88028053162511	0.02674609602650	-1.21948419952974
C	1.52293405649694	-0.33343427528994	-2.03530191128564
H	4.21069644756540	-0.08116992174710	-2.25695897577083
H	5.88562938872835	0.31195089011831	-0.46219220153284
H	2.70632876588950	0.42970364744097	2.44898463998124
H	5.12720620742351	0.57155001887274	1.90643523583420
Cl	-0.04563715446420	0.19551223857127	2.97639524305248
H	1.93070942248299	-0.05675399218475	-3.01797640896347
H	0.58380865384430	0.22408190817449	-1.88636340893037
H	1.25781621163405	-1.40254457039001	-2.07595328955707

31

Complex 2, singlet

Ni	-0.01103117652357	-0.01418090143263	0.11506774356940
Cl	2.14925586412638	-0.04521724242918	0.28498921636674
C	-0.20512451075398	1.87785786274046	0.14674556292513
N	-1.84562041328474	-0.01082811972732	-0.03671203937219
C	0.76787642010726	2.87772743832449	0.25678682545166
N	-0.27858449625194	-1.97908799003754	0.04613610644544
C	0.40706588910746	4.23342482584581	0.26420054967040
C	-0.93435257659201	4.62056510198634	0.16189117547416
C	-1.92690616781578	3.64592729013373	0.05136071510854
C	-1.56738723663318	2.29085847017269	0.04408622190700
C	-2.50404809757859	1.18167353249793	-0.06261429209395
C	-3.89795436954511	1.19685159761799	-0.17922146984213
C	-4.58966758515179	-0.01256762474759	-0.26679977071424
C	-3.89435696882500	-1.22461866142900	-0.23810513126240
C	-2.50335219350083	-1.19442872025220	-0.12093186474315
C	-1.59228667009129	-2.34022634866180	-0.07207149814790
C	-1.97960025430166	-3.67939541969995	-0.13591126845262
C	-1.00217447021527	-4.67168690201289	-0.07571619354048
C	0.33735316116038	-4.29679699536492	0.04565368376272
C	0.65751545104306	-2.94200166033455	0.10271255018075
H	1.81993099432305	2.60306268063177	0.33776155753278
H	1.18524939758338	4.99485050023774	0.35121878609848
H	-1.20390117102639	5.67753325636629	0.16849563770241
H	-2.97578261170013	3.93976152796975	-0.02781984942884
H	-4.43062905912764	2.14668064742618	-0.20020456993644
H	-5.67589223451593	-0.01307046789785	-0.35806990824491
H	-4.42303577063430	-2.17388003967309	-0.30464333010386
H	-3.03275363362856	-3.94020494264937	-0.23139559088037
H	-1.28424997117624	-5.72362253856772	-0.12347551454153
H	1.13242277080386	-5.03971576016491	0.09613886000590
H	1.68489242261941	-2.58771383186871	0.19638593510349

31

Complex 2, triplet

Ni	-0.03154259606317	-0.04186285185788	0.72949749001053
Cl	1.74369070309274	-0.20543704903873	2.02244683693068
C	-0.20548818230462	1.83396067629290	0.10283122056642
N	-1.94621818257817	-0.02880203721374	0.35834870643501
C	0.79154540000714	2.80857445819692	-0.01923080275250
N	-0.30074389805412	-1.92161677455983	0.04692416789701
C	0.45856241298278	4.16934992807500	-0.07067391958178
C	-0.88085731849639	4.57684900426040	0.00656712075486
C	-1.89596809193004	3.62653932179040	0.11989510099711
C	-1.56492457531795	2.26245963501133	0.14904638032998
C	-2.54165517353379	1.16952565590870	0.14679018184916
C	-3.90495694683604	1.20883481965833	-0.16799028800168
C	-4.59333863300189	0.00482055780579	-0.35039396614564
C	-3.91188935981580	-1.21485180203481	-0.28358044313274
C	-2.55785289784943	-1.19509724179561	0.06285214393404
C	-1.61270593710369	-2.31618514609427	0.02422298561539
C	-1.96285783927784	-3.66461080315139	-0.08104917433249
C	-0.95682884353248	-4.62175638545702	-0.18619286442216
C	0.38033041697265	-4.20893503935304	-0.17972445817040
C	0.66670627476997	-2.85393987980131	-0.05266546746641
H	1.84329800672120	2.51575997707609	-0.05786975956604
H	1.24778493436328	4.91823303621333	-0.16771793926700
H	-1.13063251388379	5.63841613950754	-0.02394357250623
H	-2.93869927256595	3.94598397288740	0.18208172699513
H	-4.40935522887317	2.16421669315402	-0.30803606083286
H	-5.65248497765686	0.01941523994668	-0.60836492327248
H	-4.41308920375999	-2.15043749632542	-0.52716413840749
H	-3.01285590405990	-3.95534928334402	-0.07586344791954
H	-1.21054792912746	-5.67861770079101	-0.26907117728843
H	1.19591156406513	-4.92555181323539	-0.26781073696651
H	1.69053452464797	-2.48235724673145	-0.01822208628295

## Tethered Ni(I)-bpy phenyl intermediate

Ni	-0.00234460923189	-0.04128906222233	0.11371342154512
C	-0.14894822625261	1.86983554015147	0.14939255069195
N	-1.88621944034923	-0.03324552770620	-0.04248196707353
C	0.78910625369256	2.91437592619919	0.25752023994391
N	-0.27203541116415	-1.97323732065526	0.04533983768199
C	0.40938188096168	4.26555971496384	0.26493763638459
C	-0.94004791274887	4.62251234169919	0.16362287599611
C	-1.90979896404278	3.62215324602436	0.05394222327886
C	-1.52643727639970	2.27352730226671	0.04694653620720
C	-2.50020188757835	1.17124618182494	-0.06335870956375
C	-3.89668863323825	1.20558079608942	-0.17942952962521
C	-4.59994779653043	-0.00275827016886	-0.26820533733959
C	-3.92870314798785	-1.23116002990575	-0.24231242899791
C	-2.53418756795815	-1.20929290366336	-0.12538213702732
C	-1.59451083509654	-2.34394907469695	-0.07338923896517
C	-1.97373222619462	-3.68484883344834	-0.13490631792620
C	-0.99914965460617	-4.68085730152242	-0.07434216090817
C	0.34104881632927	-4.30500283163362	0.04655322662339
C	0.65904952602579	-2.95063946969661	0.10207044830446
H	1.85347836215242	2.67683423560917	0.33939890532457
H	1.17065924759271	5.04503409832468	0.35060883117615
H	-1.23497332265098	5.67307221809631	0.16956541867563
H	-2.96385387251569	3.89980159415833	-0.02484285667762
H	-4.43066661907418	2.15528723266492	-0.20012460933842
H	-5.68657890751550	0.01294593382687	-0.35892559146249
H	-4.47878159971710	-2.16887276920139	-0.31037121784756
H	-3.02775042516299	-3.94437183893515	-0.22947785012779
H	-1.28201412173899	-5.73249102411070	-0.12100366211043
H	1.13705510513478	-5.04711894291870	0.09773657947011
H	1.69231267166993	-2.61609622212325	0.19606488005792